CXCR4 identifies transitional bone marrow premonocytes that replenish the mature monocyte pool for peripheral responses

Shu Zhen Chong,[1]* Maximilien Evrard,[1,2]* Sapna Devi,[1] Jinmiao Chen,[1] Jyue Yuan Lim,[1] Peter See,[1] Yiru Zhang,[3] José M. Adrover,[4] Bernett Lee,[1] Leonard Tan,[1] Jackson L.Y. Li,[1] Ka Hang Liong,[1] Cindy Phua,[1] Akhila Balachander,[1] Adrian Boey,[5] David Liebl,[5] Suet Mien Tan,[2] Jerry K.Y. Chan,[6,7,8] Karl Balabanian,[9] John E. Harris,[10] Mariaelvy Bianchini,[11] Christian Weber,[11] Johan Duchene,[11] Josephine Lum,[1] Michael Poidinger,[1] Qingfeng Chen,[3] Laurent Rénia,[1] Cheng-I Wang,[1] Anis Larbi,[1] Gwendalyn J. Randolph,[12] Wolfgang Weninger,[13] Mark R. Looney,[14] Matthew F. Krummel,[14] Subhra K. Biswas,[1] Florent Ginhoux,[1] Andrés Hidalgo,[4,11] Françoise Bachelerie,[9] and Lai Guan Ng[1,2]

[1]Singapore Immunology Network (SIgN), A*STAR (Agency for Science, Technology and Research), Biopolis, 138648 Singapore
[2]School of Biological Sciences, Nanyang Technological University, 637551 Singapore
[3]Institute of Molecular and Cell Biology (IMCB), A*STAR (Agency for Science, Technology and Research), Biopolis, 138673 Singapore
[4]Area of Cell and Developmental Biology, Fundación Centro Nacional de Investigaciones Cardiovasculares (CNIC), Madrid 28029, Spain
[5]Institute of Medical Biology (IMB)-Institute of Molecular and Cell Biology (IMCB) Electron Microscopy Suite, A*STAR (Agency for Science, Technology and Research), Biopolis, 138671 Singapore
[6]Experimental Fetal Medicine Group, Yong Loo Lin School of Medicine, National University of Singapore, 119228 Singapore
[7]Department of Reproductive Medicine, KK Women's and Children's Hospital, 229899 Singapore
[8]Cancer and Stem Cell Biology Program, Duke-NUS Graduate Medical School, 169857 Singapore
[9]INSERM UMR-S996, Laboratory of Excellence in Research on Medication and Innovative Therapeutics, Université Paris-Sud, 92140 Clamart, France
[10]Department of Medicine, University of Massachusetts Medical School, Worcester, MA 01605
[11]Institute for Cardiovascular Prevention, Ludwig-Maximilians-University Munich, Munich 80336, Germany
[12]Division of Immunobiology, Washington University, St. Louis, MO 63110
[13]Centenary Institute for Cancer Medicine and Cell Biology, Newton, New South Wales 2042, Australia
[14]Department of Medicine and Pathology, Cardiovascular Research Institute, University of California, San Francisco, San Francisco, CA 94143

It is well established that Ly6C^{hi} monocytes develop from common monocyte progenitors (cMoPs) and reside in the bone marrow (BM) until they are mobilized into the circulation. In our study, we found that BM Ly6C^{hi} monocytes are not a homogenous population, as current data would suggest. Using computational analysis approaches to interpret multidimensional datasets, we demonstrate that BM Ly6C^{hi} monocytes consist of two distinct subpopulations (CXCR4^{hi} and CXCR4^{lo} subpopulations) in both mice and humans. Transcriptome studies and in vivo assays revealed functional differences between the two subpopulations. Notably, the CXCR4^{hi} subset proliferates and is immobilized in the BM for the replenishment of functionally mature CXCR4^{lo} monocytes. We propose that the CXCR4^{hi} subset represents a transitional premonocyte population, and that this sequential step of maturation from cMoPs serves to maintain a stable pool of BM monocytes. Additionally, reduced CXCR4 expression on monocytes, upon their exit into the circulation, does not reflect its diminished role in monocyte biology. Specifically, CXCR4 regulates monocyte peripheral cellular activities by governing their circadian oscillations and pulmonary margination, which contributes toward lung injury and sepsis mortality. Together, our study demonstrates the multifaceted role of CXCR4 in defining BM monocyte heterogeneity and in regulating their function in peripheral tissues.

INTRODUCTION

Monocytes arise from common monocyte progenitors (cMoPs) in the BM (Hettinger et al., 2013) and develop into mature Ly6C^{hi} monocytes before being released into the blood. In comparison to other myeloid cells (Terashima et al., 1996), monocytes have an exceedingly short transit time through the BM and are rapidly released into the circulation after their last division (Goto et al., 2003). Upon entering the circulation, Ly-6C^{hi} monocytes have a half-life of just 20 h before undergoing terminal differentiation into longer-lived Ly6C^{lo} monocytes (with a half-life of 48 h;Varol et al., 2007; Hanna et al., 2011;

*S.Z. Chong and M. Evrard contributed equally to this paper.

Correspondence to Lai Guan Ng: Ng_Lai_Guan@immunol.a-star.edu.sg; or Shu Zhen Chong: Chong_Shu_Zhen@immunol.a-star.edu.sg

Abbreviations used: ALI, acute lung injury; CLP, cecal ligation and puncture; CMap, connectivity map; cMoP, common monocyte progenitor; DEG, differential gene expression; Fucci, fluorescence ubiquitin cell cycle indicator; IPA, ingenuity pathway analysis; NGS, next generation sequencing; OLO, optimal leaf ordering; PCA, principal component analysis; TpMo, transitional premonocytes; t-SNE, t-distributed stochastic neighbor embedding; WHIM, warts, hypogamma-globulinemia, infections, and myelokathexis; ZT, zeitgeber.

The Rockefeller University Press $30.00
J. Exp. Med. 2016 Vol. 213 No. 11 2293–2314
https://doi.org/10.1084/jem.20160800

Supplemental material can be found at:
http://doi.org/10.1084/jem.20160800

Mildner et al., 2013; Yona et al., 2013). It is therefore highly essential that circulating Ly6C^{hi} monocytes are constantly being replenished through the coordinated release of these cells from the BM. Current evidence indicates that the release of BM Ly-6C^{hi} monocytes is governed by CCR2 and CX_3CR1, with the latter receptor reportedly influencing the survival of Ly6C^{lo} monocytes (Serbina and Pamer, 2006; Landsman et al., 2009; Shi and Pamer, 2011; Jacquelin et al., 2013). CXCR4-signaling also acts as an anchoring force that retains Ly6C^{hi} monocytes in the BM (Jung et al., 2015; Liu et al., 2015), whereas its inhibition (Beaussant Cohen et al., 2012; McDermott et al., 2014) reverses the observed monocytopenia present in patients with WHIM syndrome (Warts, hypogamma-globulinemia, infections, and myelokathexis; Hernandez et al., 2003; Gulino et al., 2004).

Although circulating monocytes have historically been regarded as precursor cells that replenish tissue macrophages and DC populations (Segura and Amigorena, 2013; Varol et al., 2015), it is now increasingly being recognized that monocytes exert potent effector functions at peripheral sites throughout the body (Mildner et al., 2013). Monocytes comprise between ∼4 and 10% of total blood leukocytes and include two major subsets that participate in host defense and tissue repair (Ginhoux and Jung, 2014). In mice, Ly6C^{hi} monocytes resemble human CD14^{+}CD16^{-} classical monocytes (Cros et al., 2010; Ingersoll et al., 2010; Wong et al., 2011) that express multiple cytokines and granule-associated proteins for effector functions at infectious and inflammatory sites (Serbina et al., 2008). In contrast, murine Ly6C^{lo} monocytes resemble human CD14^{-}CD16^{+} nonclassical monocytes (Cros et al., 2010; Ingersoll et al., 2010) that patrol and eliminate cellular debris from blood vessel walls (Auffray et al., 2007; Carlin et al., 2013), as well as control tumor metastasis in the lung (Hanna et al., 2015). In addition, several studies have shown that monocytes mediate the recruitment of leukocytes in response to pathological insults (Kreisel et al., 2010; Carlin et al., 2013), and are essential for peripheral tissue repair during the resolution phase (Nahrendorf et al., 2010). Consequently, their ability to be rapidly mobilized from the BM for their deployment to inflammatory sites, as well as to return to a state of homeostasis, is critical for effective immune responses and prevention of collateral tissue damage. Furthermore, monocytes are progressively being recognized as attractive targets for therapeutic interventions, as lipid nanoparticles and antagonists that target monocytes have shown therapeutic efficacy in several diseases (Leuschner et al., 2011; Majmudar et al., 2013; Poupel et al., 2013). It is therefore imperative that a better understanding of their cellular and molecular mechanisms be explored at multiple tissue levels.

Using a combination of computational analysis approaches coupled with transcriptome profiling and in vivo assays, we identify a previously unknown heterogeneity that exists among BM Ly6C^{hi} monocytes in both human and mice. Specifically, BM Ly6C^{hi} monocytes consist of two distinguished subpopulations (CXCR4^{hi} and CXCR4^{lo} subpopulations) and that the immobilized CXCR4^{hi} subset serves as a transitional precursor for the replenishment of mature CXCR4^{lo} monocytes. Additionally, we provide new insights into the role of CXCR4 in mediating the spatiotemporal localization of monocytes in peripheral sites by demonstrating its role in diurnal oscillations and pulmonary margination. Importantly, disruption of CXCR4-signaling also led to reduced lung injury and sepsis mortality. Together, our findings identify a previously undefined developmental transition that exists among BM Ly6C^{hi} monocytes and demonstrates the multifaceted role of CXCR4 in their peripheral tissue responses.

RESULTS

CXCR4 defines heterogeneity among BM Ly6C^{hi} monocytes

It is now well established that cMoPs give rise to Ly6C^{hi} monocytes in the BM (Hettinger et al., 2013). However, it is unclear whether BM Ly6C^{hi} monocytes consist of a homogenous population or if further heterogeneity exists among these cells. To address this question, we analyzed BM Ly6C^{hi} monocytes (excluding their progenitors) using an unsupervised dimensional reduction algorithm (distributed stochastic neighbor embedding [t-SNE]; Amir et al., 2013; Becher et al., 2014) on flow cytometry data based on six common myeloid cell markers, CXCR4, CD31, CD16/32, CX_3CR1, CCR2, and CD11b (Fig. 1 A). This approach allows us to visualize multidimensional similarities of cells in a 2D scatter plot, known as the t-SNE map, which results in enhanced visualization of small cellular subpopulations through cell clusters with similar protein expression patterns (Amir et al., 2013; Becher et al., 2014). Visualization of BM Ly6C^{hi} monocytes on the t-SNE map revealed heterogeneity among these cells, which can be categorized into two main subsets through automated clustering (Fig. 1 A). Upon examination of each selected marker, we found that CXCR4 delineated BM Ly-6C^{hi} monocytes into two subsets that closely represented the outcome generated by automated clustering (Fig. 1 B). Furthermore, CXCR4 segmentation resulted in the highest ratio in median intensity between these two clusters (Fig. 1 C), suggesting that CXCR4 could serve as a suitable surface marker in delineating BM Ly6C^{hi} monocyte heterogeneity. Indeed, we found two distinct populations of Ly6C^{hi} monocytes in the BM that consisted of a CXCR4^{hi} and CXCR4^{lo} subset (Fig. 1 D). Furthermore, scanning electron microscopy revealed morphological differences between these two subsets, with only the CXCR4^{lo} subset protruding its cytoplasmic membrane upon adhering to coverslips (Fig. 1 E). We also validate the presence of CXCR4-defined heterogeneity among human BM monocytes and observed the presence of CXCR4^{hi} and CXCR4^{lo} monocytes (Fig. 1 F). Collectively, our results identify heterogeneity in the current established BM Ly6C^{hi} monocyte pool and the presence of a distinct subpopulation that can be delineated through CXCR4.

Transcriptome profiling reveals distinct gene expression signatures between BM CXCR4^{hi} and CXCR4^{lo} Ly6C^{hi} monocytes

To further characterize the CXCR4^{hi} and CXCR4^{lo} monocyte subsets, we sorted all cells in the monocyte

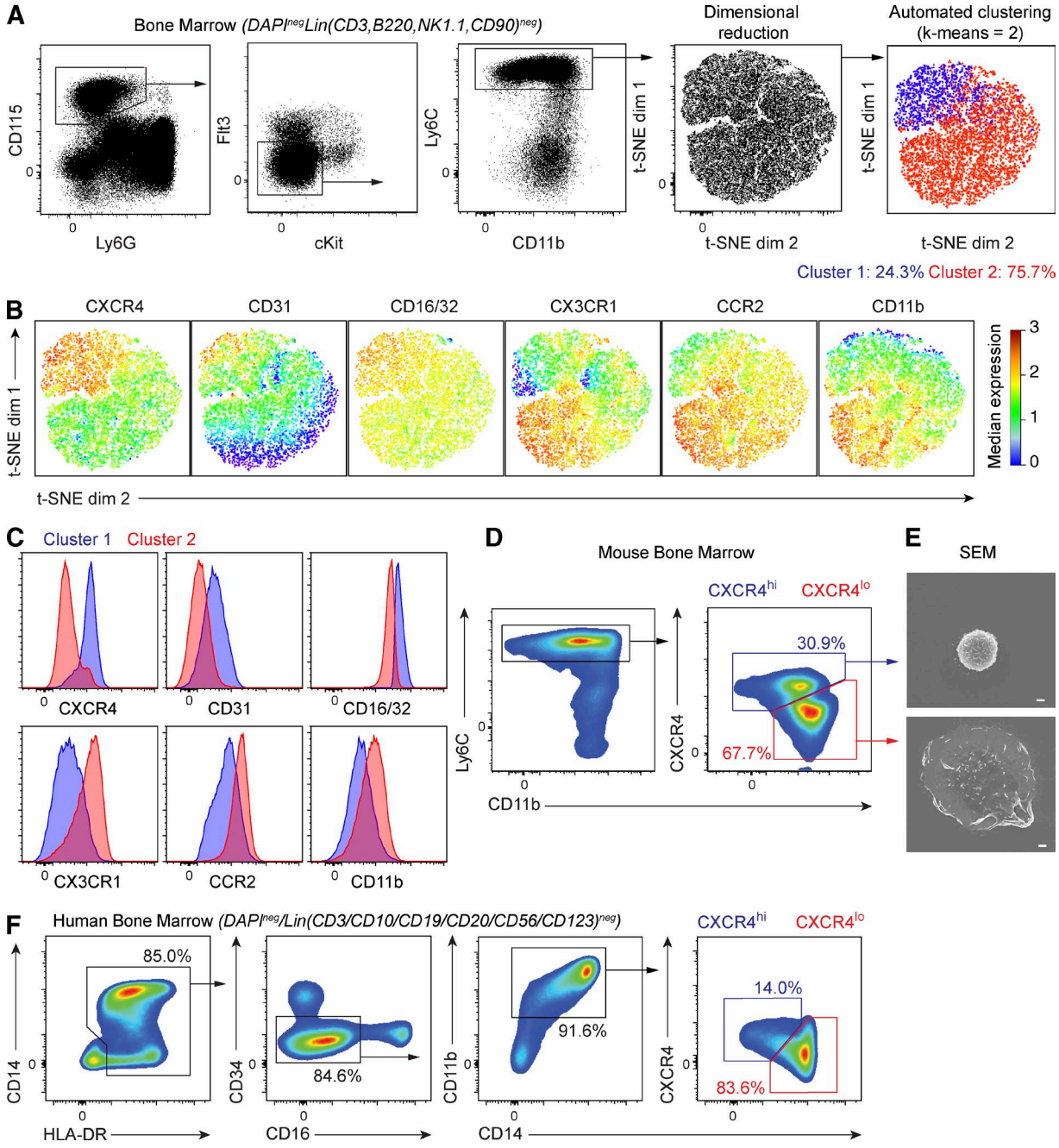

Figure 1. **CXCR4 defines heterogeneity among BM Ly6C^{hi} monocytes.** (A) BM Ly6C^{hi} monocytes were gated accordingly (left) and subjected to t-SNE dimensional reduction (middle). Automatic clustering was performed using k-means, and clusters plotted into the t-SNE map (right). (B) Indicated markers are color mapped from blue (low expression) to red (high expression) into the t-SNE map. (C) Overlayed histograms of indicated markers constructed from data obtained from the k-means of cluster 1 (blue) and cluster 2 (red) that was generated from automated clustering. (A–C) Data are representative of one out of three experiments with at least $n = 3$ samples. (D–E) BM Ly6C^{hi} monocytes in mice divided into CXCR4^{hi} (blue) and CXCR4^{lo} (red) subsets (D) with scanning electron microscopy images of mouse CXCR4^{hi} (top) and CXCR4^{lo} (bottom) subsets (E). Bars, 1 µm. Data are representative of one out of three experiments. (F) Gating strategy and division of human BM classical monocytes into CXCR4^{hi} (blue) and CXCR4^{lo} (red) subsets. Data are representative of one out of three experiments conducted with seven independent donors.

developmental pathway, specifically cMoPs, CXCR4^{hi}, and CXCR4^{lo} Ly6C^{hi} monocyte subsets, and Ly6C^{lo} monocytes from the BM (Fig. 2 A). Subsequently, we performed whole transcriptome sequencing using next generation sequencing (NGS) on these cells to compare their genome-wide RNA expression profiles. Princi-

pal-component analysis (PCA) of all expressed genes revealed distinct and well-separated transcriptomic profiles (Fig. 2 B), implying that the CXCR4^{hi} subpopulation was clearly distinct from all other monocyte subsets in the BM. In particular, comparative analysis of cMoP and the CXCR4^{hi} subset revealed an enrichment of genes in the CXCR4^{hi} subset that was predominantly associated with cell migration and monocyte function, such as *Fn1*, *Vcan*, *Ccr1*, *Lyz2*, and *Msr1* (Fig. 2 C). In contrast, cMoPs displayed an enrichment of self-renewal genes, such as *Cd34* and *Kit*, and neutrophil-associated microbicidal activity genes such as *Mpo*, *Ctsg*, and *Elane* (Fig. 2 C). Comparative analysis of the CXCR4^{hi} to CXCR4^{lo} subset also revealed a significantly large enrichment of cell cycle–dependent genes in the CXCR4^{hi} subset, such as *Ccnf*, *Top2a*, *Mki67* and *Cdk1*. In contrast, the CXCR4^{lo} subpopulation displayed an enrichment of monocyte effector function genes such as *Cd14*, *C5ar1*, *Nod2*, and *Il1b* (Fig. 2 C). Biofunction enrichment analysis using Ingenuity pathway analysis (IPA; Fig. 2 D) and heat maps (Fig. S1) of gene expression data further confirmed these findings. In particular, the CXCR4^{hi} subset was found to be functionally more mature than cMoPs but less mature than the CXCR4^{lo} subset. We also discovered several candidate surface markers that allow the discrimination of the CXCR4^{hi} subset from the CXCR4^{lo} subset and cMoPs (Fig. 2 E and Fig. S2).

Although BM Ly6C^{hi} monocytes have been thought to be terminally differentiated cells that proliferate minimally in the steady state (van Furth et al., 1979), the enrichment of cell cycle genes in the CXCR4^{hi} subset prompted us to determine if these cells may proliferate in vivo. To address this, we used a fluorescence ubiquitin cell cycle indicator (Fucci) transgenic mouse that labels for cells in the S and G2/M phase of the cell cycle. Although the CXCR4^{lo} subset and Ly6C^{lo} monocytes were not fluorescent for Fucci, the CXCR4^{hi} subset and cMoP were found to be Fucci^{+} and actively cycling in the S/G2/M phase (Fig. 2 F). BrdU incorporation assays further revealed that the majority of cells belonging to the CXCR4^{hi} subset were in the S phase of the cell cycle, in contrast to the CXCR4^{lo} subset that was in the G0/G1 phase (Fig. 2 G). Furthermore, we made similar observations in human BM cells (Fig. 2 H). Specifically, the CXCR4^{hi} subset was found to be actively replicating in the S phase of the cell cycle through BrdU incorporation in vitro and expressed slightly lower levels of CD14 and CD11b but higher levels of HLA-DR (Fig. 2 H). To complement our phenotypic studies, we performed an in vivo bead uptake assay and confirmed that the CXCR4^{hi} subset was functionally less active than the CXCR4^{lo} subset through reduced bead uptake in vivo (Fig. 2 I). Collectively, our data distinguishes the CXCR4^{hi} subset as a distinct subpopulation that differs phenotypically and functionally from the CXCR4^{lo} subset of Ly6C^{hi} monocytes.

Identification of a developmental relationship between BM Ly6C^{hi} monocyte subpopulations

To understand how the newly identified CXCR4^{hi} subset may relate to monocyte development in the BM, we first compared the transcriptomic signature of the CXCR4^{hi} subset with signatures specific for both Ly6C^{hi} and Ly6C^{lo} monocytes by Connectivity map (CMap) analysis (Fig. 3 A). Notably, the CMap analysis is a gene-set enrichment analysis algorithm that generates indicative scores of closeness to one cell subset of a defined signature gene set (Lamb et al., 2006). CMap analysis revealed a skewing of transcriptomic characteristics of the CXCR4^{hi} subset toward the Ly6C^{hi} but not Ly6C^{lo} monocyte signature, suggesting that the CXCR4^{hi} subset may be an intermediate precursor that bridges the cMoP and the CXCR4^{lo} subset (Fig. 3 A). Furthermore, optimal leaf ordering (OLO; Bar-Joseph et al., 2001) of transcriptomic data obtained from cMoP, CXCR4^{hi}, and CXCR4^{lo} Ly6C^{hi} monocytes produced a dendrogram that supports the appearance of the CXCR4^{hi} subset before the development of the CXCR4^{lo} subset (Fig. 3 B). To further understand the developmental relationship and phenotypic changes that may occur between the CXCR4^{hi} and CXCR4^{lo} subsets, we used the *Wanderlust* algorithm, which orders single cells according to their most immature to mature state into a constructed trajectory (Bendall et al., 2014). Based on FACS data that consisted of six parameters indicated in Fig. 1 B, we selected the starting point as cells that expressed high levels of CXCR4, CD31, and CD16/32 as observed on cMoPs (Fig. 2 E). Based on these data, the *Wanderlust* algorithm computationally determined early events (i.e., immature cells) as CXCR4^{hi}CD11b^{lo}CCR2^{lo}CX$_3$CR1^{lo} cells, whereas late events (i.e., mature cells) consisted of CXCR4^{lo}CD11b^{hi}CCR2^{hi}CX$_3$CR1^{hi} cells (Fig. 3 C). Furthermore, we found that CXCR4, CD31, and CD16/32 were down-regulated, whereas CCR2, CX$_3$CR1, and CD11b were up-regulated during the course of BM Ly6C^{hi} monocyte maturation (Fig. 3 D). These results hence strongly suggest that the CXCR4^{hi} subset may be a precursor of the mature CXCR4^{lo} subset. To confirm these findings in vivo, we adoptively transferred sorted CXCR4^{hi} BM Ly6C^{hi} monocytes into recipient mice and observed that the CXCR4^{hi} subset differentiated into the CXCR4^{lo} subset (Fig. 3 E). Moreover, administration of BrdU into mice, which allowed us to track the maturation of these cells, further confirmed the CXCR4^{hi} subset as an immediate precursor of the CXCR4^{lo} subset (Fig. 3 F). Notably, we did not detect the presence of Ly6C^{lo} monocytes upon the appearance of Ly6C^{hi} monocytes in these experiments (unpublished data). We also provide evidence that CXCR4 is critically linked to BM Ly6C^{hi} monocyte maturation and that the CXCR4^{lo} subset represents mature Ly6C^{hi} monocytes that eventually egress into the bloodstream during homeostatic conditions (Fig. 3, G and H; and Fig. S3). Collectively, our results describe a previously undefined developmental pathway of monocytes and that the CXCR4^{hi} subset acts as an immediate precursor of mature Ly6C^{hi} monocytes.

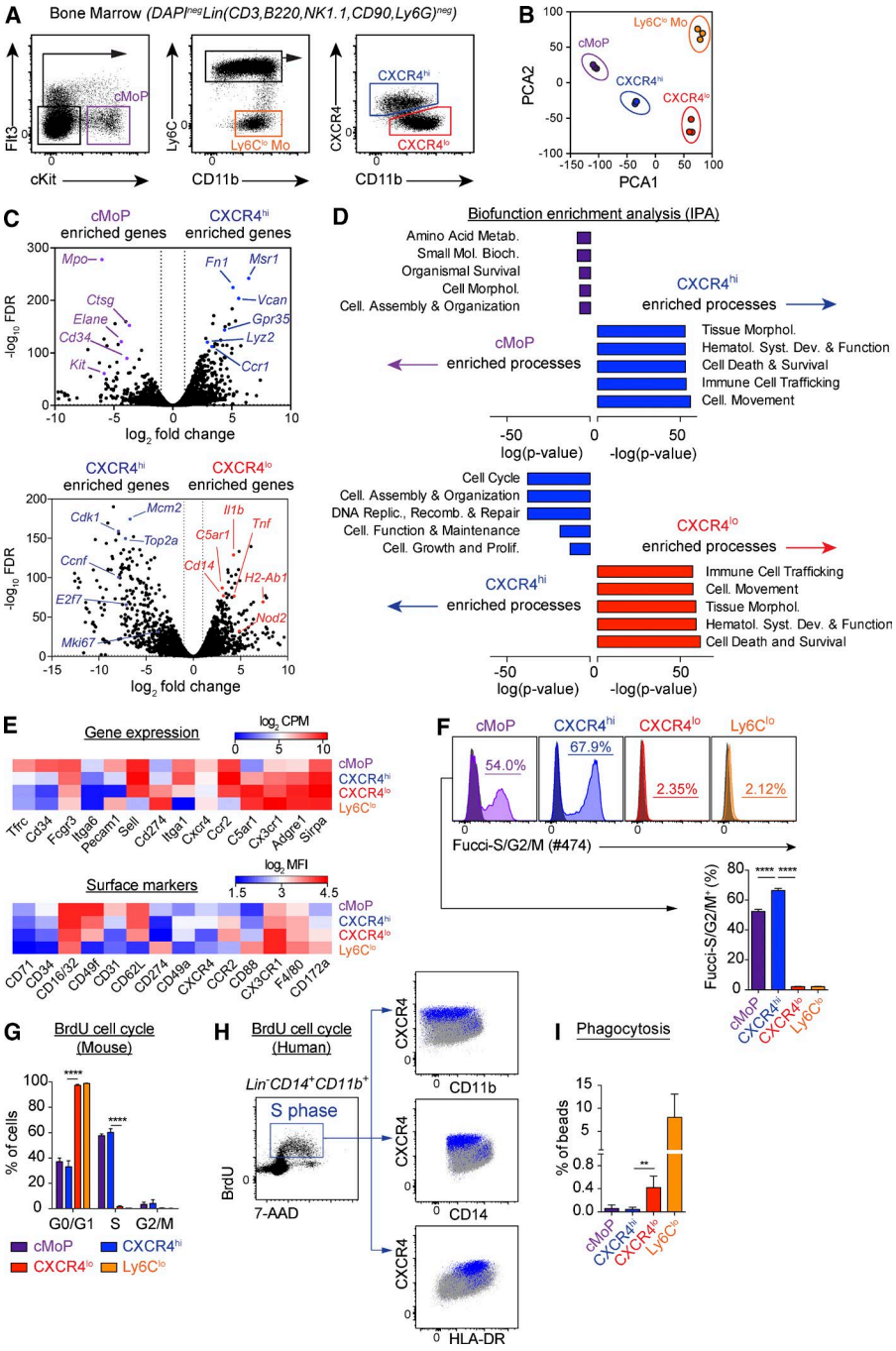

Figure 2. **Transcriptomics reveal distinct expression signatures between the CXCR4^{hi} and CXCR4^{lo} Ly6C^{hi} monocyte populations.** (A–E) BM cMoP, CXCR4^{hi}, and CXCR4^{lo} Ly6C^{hi} subsets and Ly6C^{lo} monocytes were sorted from three individual mice according to the gating strategy (A), and then RNA extracted for NGS. (B) PCA of gene expression. (C) Volcano plots depicting the $\log_2$ fold change between cMoP and CXCR4^{hi} subset (top) and CXCR4^{hi} and CXCR4^{lo} subset (bottom) versus the $-\log_{10}$ FDR. (D) Biofunction enrichment analysis of the top gene-ontology processes that are enriched when comparing cMoP versus CXCR4^{hi} subset (top) and CXCR4^{hi} versus CXCR4^{lo} subset (bottom) using IPA. (E) Heat maps of gene expression ($\log_2$ CPM; top) and surface markers validated by flow cytometry ($\log_2$ MFI; bottom). Flow cytometry data are representative of one out of three experiments. (F) Frequency of proliferating cells among BM monocyte subsets determined by Fucci-474 mice in vivo. Numbers in histograms (top) represent percentage of proliferating cells. Results (bottom) are expressed as mean ± SD (n = 3) and representative of two independent experiments. ****, $P < 0.0001$ (one-way ANOVA). (G) Mouse monocyte subsets in cell cycle stages assessed through BrdU incorporation in vivo. Results are expressed as mean ± SD (n = 5) and representative of two independent experiments. ****, $P < 0.0001$ (one-way ANOVA). (H) Human BM cells were pulsed with 10 µM of BrdU in vitro and monocytes in the S phase (left) were found to be CXCR4^{hi}, CD11b^{lo}, CD14^{lo}, and HLA-DR^{hi} (right). Results are representative of one out of four independent donors. (I) BM mouse monocytes subsets were assessed for their uptake of microspheres in vivo after 4 h through flow cytometry. Results are expressed as mean ± SD (n = 5) and representative of two independent experiments. **, $P < 0.01$ (one-way ANOVA).

The CXCR4^{hi} subset functions as a transitional precursor for the replenishment of active CXCR4^{lo} mature Ly6C^{hi} monocytes

The circadian rhythmic release of immune cells, in particular hematopoietic stem cell progenitors and monocytes, from the BM into the circulation represents a fundamental physiological process that is integral for host defense and homeostasis (Nguyen et al., 2013; Scheiermann et al., 2013). Because our current results identify BM Ly6C^{hi} monocytes as a heterogeneous population (Figs. 1, 2, and 3), we therefore examined their behavior at different periods of the circadian rhythm. Here, we observed that only the mature CXCR4^{lo} subset, but not the CXCR4^{hi} subset, cMoP, or Ly6C^{lo} monocytes, in the BM oscillated in numbers according to the circadian rhythm (Fig. 4 A). Although the CXCR4^{hi} subset did not exhibit changes in CXCR4 expression, the CXCR4^{lo} subset exhibited lower CXCR4 expression and a reduced number in the BM at ZT5 (zeitgeber 5; 5 h after the onset of light) and a higher CXCR4 expression and number at ZT13 (at the beginning of the active phase; Fig. 4 B). These results

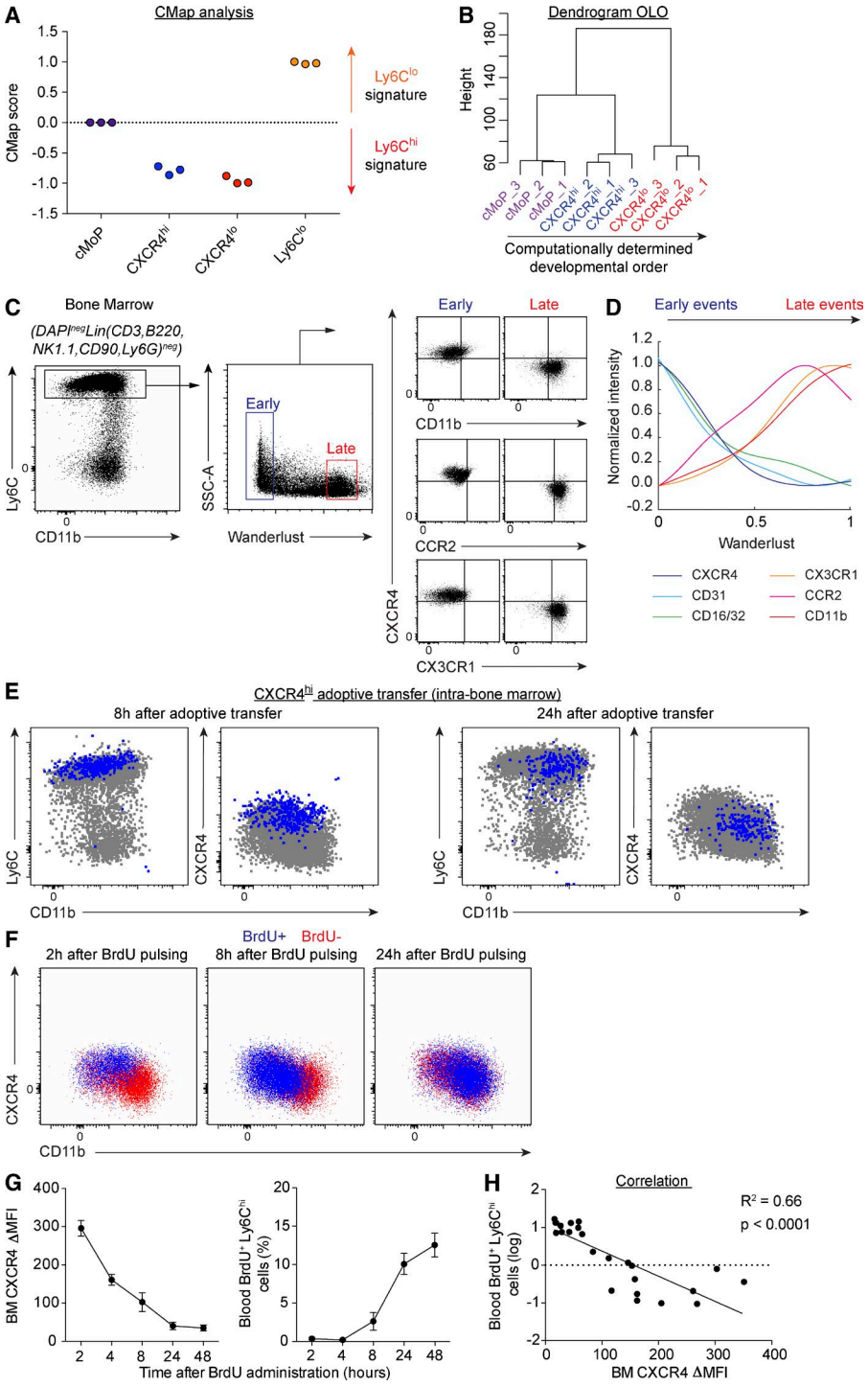

Figure 3. **Identification of a developmental relationship between subpopulations of BM Ly6C^{hi} monocytes.** (A) CMap analysis of cMoP, CXCR4^{hi} subset, CXCR4^{lo} subset, and Ly6C^{lo} monocytes displaying their enrichment for Ly6C^{hi} or Ly6C^{lo} monocyte gene sets. (B) OLO reveals a computationally determined developmental order that starts with the cMoP and ends with the CXCR4^{lo} subset as the most mature cell type. (A and B) Data were analyzed using transcriptomic data obtained from three individual mice. (C and D) BM Ly6C^{hi} monocytes subjected to the *Wanderlust* algorithm using flow cytometry data of six parameters. Data are representative of one out of three independent experiments. (C) Events were plotted against the *wanderlust* parameter with low and high values representing early and late predicted events, respectively. Early and late events were next plotted for CXCR4 expression against CD11b, CCR2, and CX3CR1. (D) *Wanderlust* traces showing low CXCR4, CD31, and CD16/32 during the early trajectory (0–0.5), and an increase in CX3CR1, CCR2, and CD11b during the late trajectory (0.5–1). (E) Intrafemoral transfer of sorted CD45.1^{+} CXCR4^{hi} subset into CD45.2 recipients. Blue dots represent transferred cells after 8 and 24 h. Results are representative of one out of five mice in three independent experiments. (F) FACS plots of BrdU^{+} (blue) and BrdU^{-} (red) Ly6C^{hi} monocytes after BrdU administration. Results are representative of one out of five independent mice. (G) Alteration in CXCR4 expression over time among BM Ly6C^{hi} monocytes (left) and percentage of BrdU^{+} Ly6C^{hi} monocytes in the blood (right) at various time points. ΔMFI was calculated by subtracting the CXCR4 MFI of BrdU^{-} Ly6C^{hi} monocytes from that of BrdU^{+} Ly6C^{hi} monocytes (as described in Fig. S3). Results are expressed as mean ± SEM (n = 5) and representative of one out of two independent experiments. (H) Graph showing correlation between blood BrdU^{+} Ly6C^{hi} monocytes and ΔMFI of CXCR4 in the BM. Each dot represents one data time point and significance was determined using a Pearson correlation test.

hence suggest that both subsets of monocytes may display a difference in their mobilizing capacity. Therefore, we next determined how a strong mobilizing cue, such as LPS (Shi et al., 2011; Evrard et al., 2015), may impact their mobilization. Intriguingly, we observed that LPS administration resulted in the egress of the CXCR4^{lo} subset and Ly6C^{lo} monocytes, but not the CXCR4^{hi} subset and cMoP in the BM (Fig. 4, C and D). Further analysis demonstrated that the CXCR4^{hi} subpopulation displayed a much lower surface expression of CCR2 (Fig. 4 E), which led to a drastically poorer migration toward the cognate ligand CCL2 (Fig. 4 F). Together with our transcriptomic and functional data (Fig. 2), our results hence indicate that the CXCR4^{hi} subpopulation is essentially immobilized in the BM under both homeostatic and inflam-

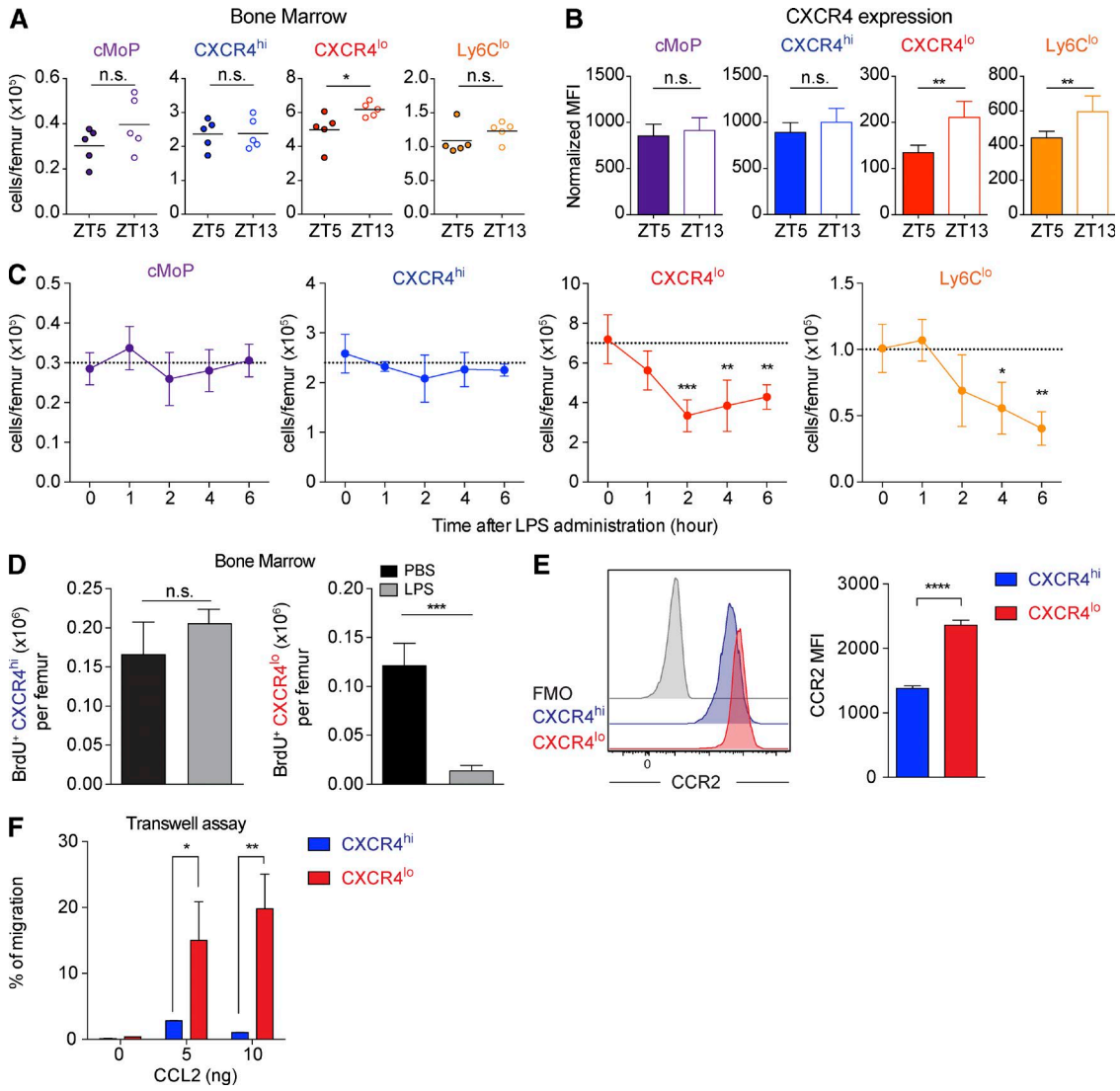

Figure 4. **BM Ly6C^{hi} monocyte subpopulations represent two distinct mobilizable pools.** (A and B) BM monocyte subsets (cMoP, CXCR4^{hi} and CXCR4^{lo} Ly6C^{hi} monocytes, and Ly6C^{lo} monocytes) were quantified for their numbers (A) and their normalized CXCR4 MFI (B) at ZT5 and ZT13. Results are expressed as mean ± SD (n = 4–5) and representative of one out of three experiments. ns, not significant; *, P < 0.05; **, P < 0.01 (Student's t test). (C) BM monocyte subset counts after LPS administration. Results expressed as mean ± SD (n = 5) and representative of one out of five independent experiments. *, P < 0.05; **, P < 0.01; ***, P < 0.001 (one-way ANOVA). (D) BrdU$^+$ CXCR4^{hi} and CXCR4^{lo} subset counts after 2 h of LPS administration. Results expressed as mean ± SD (n = 5) and representative of one out of three independent experiments. ns, not significant; ***, P < 0.001 (Student's t test). (E) CCR2 expression (left) and CCR2 MFI (arbitrary units; right) of CXCR4^{hi} and CXCR4^{lo} subsets. Results are expressed as mean ± SEM (n = 5). ****, P < 0.0001 (Student's t test). (F) Chemotaxis assay of CXCR4^{hi} and CXCR4^{lo} subsets towards CCL2. Results expressed as mean ± SD (n = 5) and representative of two independent experiments. *, P < 0.05; **, P < 0.01 (two-way ANOVA).

matory conditions to serve as a transitional precursor for the replenishment of CXCR4^{lo} mature monocytes.

CXCR4 mediates circadian rhythmic oscillations of mature monocytes and their homing into reservoirs

In contrast to the heterogeneity observed in the BM, we found that circulating Ly6C^{hi} monocytes (Fig. S4) were exclusively CXCR4^{lo}CD11b^{hi} cells (Fig. 5 A). However, it remains unclear if the reduced expression of CXCR4 upon their exit from the BM indicates its diminished role in peripheral tissue compartments. Because BM CXCR4^{lo}Ly6C^{hi} monocytes was found to exhibit diurnal fluctuations in CXCR4 expression (Fig. 4, A and B), we hence examined whether such physiological and cellular rhythms could also occur among circulating monocytes. We also determined if CXCR4 mediates these physiological processes by studying their diurnal oscillations in a conditional knockout mouse (*Lyz2^{cre}Cxcr4^{fl}* mice) that permits efficient and selective deletion of the *Cxcr4* gene

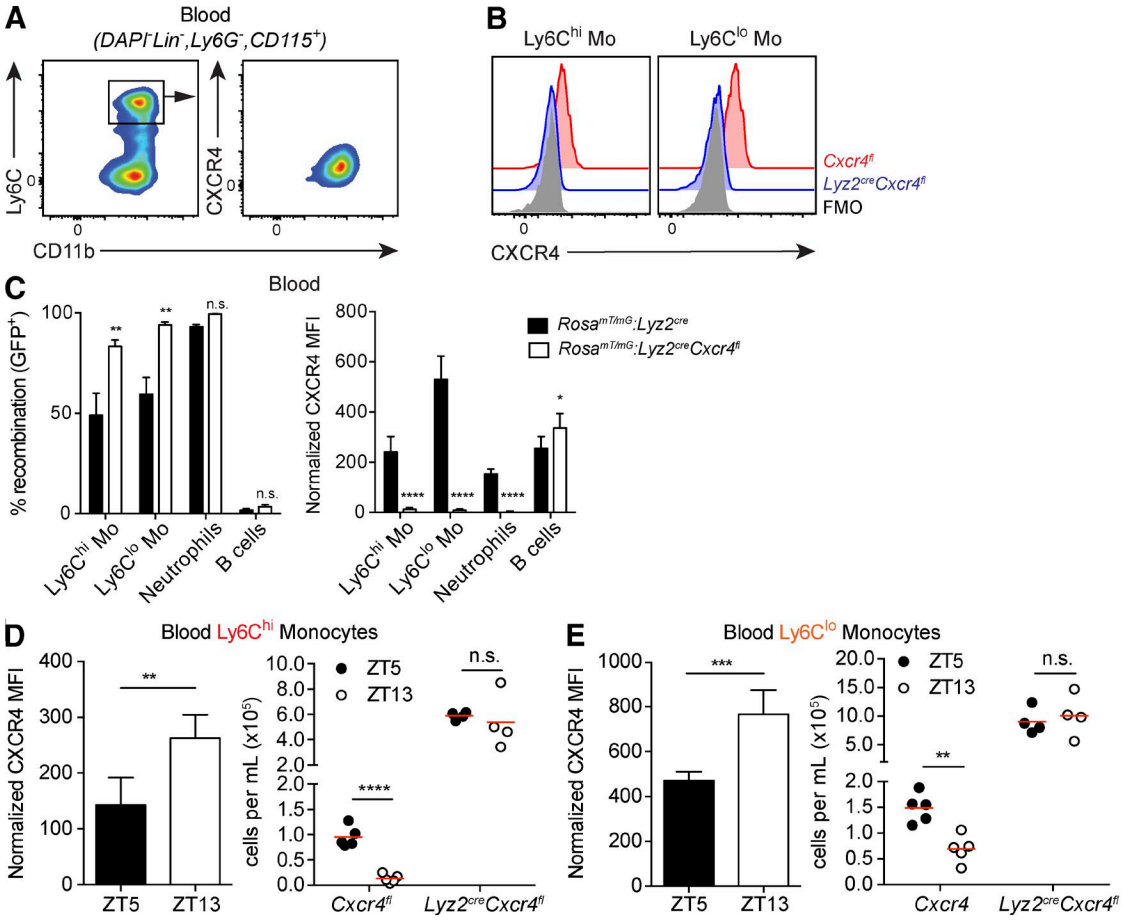

Figure 5. **CXCR4 regulates circadian rhythmic oscillations of monocytes.** (A) Representative FACS plot of CXCR4 and CD11b expression by blood Ly6C^{hi} monocytes (gating strategy in Fig. S4) of one out of four independent experiments. (B) Representative FACS plot depicting loss of CXCR4 expression in *Lyz2^{cre}Cxcr4^{fl}* mice (blue) as compared with *Cxcr4^{fl}* controls (red) of one out of three independent experiments. (C) Comparison of blood leukocyte populations in *Rosa$^{mT/mG}$:Lyz2^{cre}* mice and *Rosa$^{mT/mG}$:Lyz2^{cre}Cxcr4^{fl}* mice showing the percentage of Lyz2-cre mediated recombination (GFP$^+$) at the *Rosa26* locus (left) and normalized CXCR4 MFI (arbitrary units) of circulating leukocyte subsets (right). Results are expressed as mean ± SD (n = 4–5 mice per group). ns, not significant; *, P < 0.05; **, P < 0.01; ****, P < 0.0001 (two-way ANOVA). (D and E) Blood Ly6C^{hi} (D) and Ly6C^{lo} (E) monocyte values of normalized CXCR4 MFI on *Cxcr4^{fl}* control mice (left) and counts between *Cxcr4^{fl}* control and *Lyz2^{cre}Cxcr4^{fl}* mice (right) were quantified at ZT5 and ZT13. Data are representative of one out of three experiments. Results are expressed as mean ± SD (n = 5 mice per group). ns, not significant; **, P < 0.01; ***, P < 0.001; ****, P < 0.0001 (Student's t test).

in myeloid lineage cells, such as monocytes and neutrophils (Clausen et al., 1999; Fig. 5, B and C). Indeed, we found that circulating monocytes exhibited fluctuations in CXCR4 expression (Fig. 5, D and E) that corresponded to the high and low number of circulating Ly6C^{hi} (Fig. 5 D) and Ly6C^{lo} monocytes (Fig. 5 E) at ZT5 and ZT13, respectively. More importantly, this diurnal oscillation in monocyte numbers was abrogated in the absence of CXCR4 (Fig. 5, D and E) and highlights the role of CXCR4 in mediating the diurnal variations in circulating monocyte numbers.

Although it is likely that circadian-mediated fluctuations in CXCR4 expression could influence the release of monocytes from the BM and impact on the overall numbers of circulating monocytes, we hypothesize that this process may also act on the trafficking patterns of monocytes in peripheral compartments. To test this hypothesis, we established parabiosis between CD45.1 WT mice and CD45.2 CXCR4 genetic-modified mice (Fig. 6, A and B). CXCR4 genetic-modified mice included either *Lyz2^{cre}Cxcr4^{fl}* mice or a knock-in mouse strain that carries a *CXCR4* gain-of-function mutation characteristic of WHIM patients (termed *Cxcr4^{WHIM}* or WHIM mice; Balabanian et al., 2012; Beaussant Cohen et al., 2012; McDermott et al., 2014). The homing ratio of cells were then calculated (Fig. 6 A) to normalize for their chimerism (Fig. 6 C). Using this approach, we observed a significant decrease in the homing of *Lyz2^{cre}Cxcr4^{fl}* monocytes to the BM (Fig. 6 A). This trend was similarly observed with neutrophils (Fig. 6 A) and is consistent with the known requirement of CXCR4 in mediating their homing to the BM (Martin et al., 2003; Suratt et al., 2004; Devi et al., 2013).

In contrast, no significant differences in T cell homing ratio were observed between the *Lyz2*^{cre}*Cxcr4*^{fl} and WT parabionts as T cells are not targeted by the *Lyz2*^{cre}-mediated deletion of CXCR4 (Eash et al., 2009; Fig. 6 A) and confirms that our earlier observations on monocytes are cell intrinsic and specifically mediated by CXCR4. In contrast, WHIM mice exhibited a corresponding increase in monocyte homing to the BM in their WT partners (Fig. 6 B). Adoptive transfer experiments further confirmed these findings, as CD45.1 BM monocytes that were transferred into CD45.2-recipient mice were observed to rapidly decline in the blood and accumulate in the BM via a mechanism that was disrupted by AMD3100 treatment (Fig. 6, D and E). Interestingly, we also observed a significant decrease in the homing of *Lyz2*^{cre}*Cxcr4*^{fl} monocytes into the spleen (Fig. 6 A). Conversely, there was a trend toward an increased homing of WHIM monocytes into the spleen (Fig. 6 B). Collectively, our data highlights a role for CXCR4 in mediating the circadian rhythmic fluctuations in the overall number of circulating Ly6C^{hi} monocytes and their homing into tissue reservoirs.

Circulating monocytes accumulate in the pulmonary vasculature after endotoxin exposure

It is well established that LPS administration is a potent mediator that mobilizes monocytes from the BM, and consequently results in increased circulating monocyte numbers (Shi et al., 2011; Evrard et al., 2015). However, we consistently observed a transient phase of monocytopenia in the blood that occurs one hour after LPS administration (Fig. 7 A), which corresponded to a time point whereby no significant changes in monocyte numbers were detected in the BM (Fig. 4 C). These results hence suggest that blood monocytes were possibly being withdrawn temporarily from the circulation into other tissues. To address this hypothesis, we adopted an intravascular staining protocol (Reutershan et al., 2005; Ng et al., 2011; Anderson et al., 2014; Fig. 7 B), which allowed discrimination between intravascular or extravascular cell distributions in tissues in vivo. In the lung, this approach confirmed the extravascular location of alveolar macrophages, whereas monocytes and neutrophils were identified as being intravascular (Fig. 7 C). Using this method, we found that the LPS-induced decrease in circulating monocytes was accompanied by a gradual accumulation of these cells in the intravascular compartment of the lung (Fig. 7, D and E), with limited monocyte sequestration into other major organs (spleen, liver, and kidney; unpublished data). Furthermore, this phenomenon was mediated by the intrinsic sensing of LPS by monocytes and not vascular stromal cells, as our BM chimeric data demonstrated an abrogation of monocyte accumulation in the lung in the absence of TLR4 in the hematopoietic compartment (Fig. 7 F). Therefore, these data suggests that circulating monocytes are transiently withdrawn from the circulation and sequestered into the lung microvasculature in response to systemic inflammatory stimuli.

CXCR4 regulates monocyte margination in the pulmonary vasculature

To delineate the mechanism of LPS-induced monocyte accumulation in the lung, we used intravital two-photon microscopy to visualize the pulmonary microvasculature of *Cx3cr1*$^{gfp/+}$ reporter mice. Endotoxin exposure stimulated blood monocytes to alter their morphology and decrease their velocity in the lung capillaries, which are characteristic features of margination (Doerschuk et al., 1993; Kuebler and Goetz, 2002; Looney and Bhattacharya, 2014; Fig. 8 A and Video 1). Because lung endothelial cells express CXCL12 (Devi et al., 2013), we speculated that the CXCL12–CXCR4 signaling axis might be involved in monocyte margination in the lung. To test this hypothesis, we treated *Cx3cr1*$^{gfp/+}$ mice with AMD3100 and observed monocytes traveling through the lung microcirculation at a higher velocity and with significant reduced adherence to the endothelium, even in mice that were treated with the promargination stimulus LPS (Fig. 8, B and C; and Video 1). FACS analysis further supported these data, as shown by increased accumulation of lung monocytes in WHIM mice after LPS challenge, whereas this phenomenon was abrogated in *Lyz2*^{cre}*Cxcr4*^{fl} mice (Fig. 8 D). Because it is well known that Ly6C^{hi} monocytes also express lower levels of GFP in *Cx3cr1*$^{gfp/+}$ mice (Auffray et al., 2007), we ensured that our approach was able to detect Ly6C^{hi} monocytes during intravital imaging by administering an anti-Ly6B.2 antibody into *Cx3cr1*$^{gfp/+}$ mice to stain these cells in vivo (Fig. 8, E and F; and Video 2) and confirmed that our imaging approach accounted for these cells.

We next further determined whether CXCR4 regulated monocyte margination equally in both subsets. By using a lung efflux assay to quantify monocyte release from the pulmonary circulation (Devi et al., 2013; Fig. 9 A) without the interference from interposing organs (Bierman et al., 1952), we observed that AMD3100 treatment increased the net release of both Ly6C^{hi} and Ly6C^{lo} monocytes from the lungs (Fig. 9 B). However, only the Ly6C^{hi} subset displayed a significant increase in lung retention following LPS and this process could be prevented with the preadministration of AMD3100 (Fig. 9 B). To extend these findings in the context of humans, we found that AMD3100 also markedly increased circulating CD14^{+}CD16^{-} classical monocytes in humanized mice, which was accompanied by an increased net release of these cells from the pulmonary circulation (Fig. 9, C and D). This phenomenon was similarly observed in an experimental model of non-human primates (Fig. 9 E).

The accumulation of myeloid cells in the lung is a hallmark of injury in pulmonary diseases (MacNee and Selby, 1993). It is thus likely that an increase in margination in the lung endothelium may predispose toward tissue injury. To test this hypothesis, we used a model of acute lung injury (ALI; O'Dea et al., 2009) and found that *Lyz2*^{cre}*Cxcr4*^{fl} mice displayed a significant decrease in vascular leakage compared with the *Cxcr4*^{fl} control mouse (Fig. 9 F). Further-

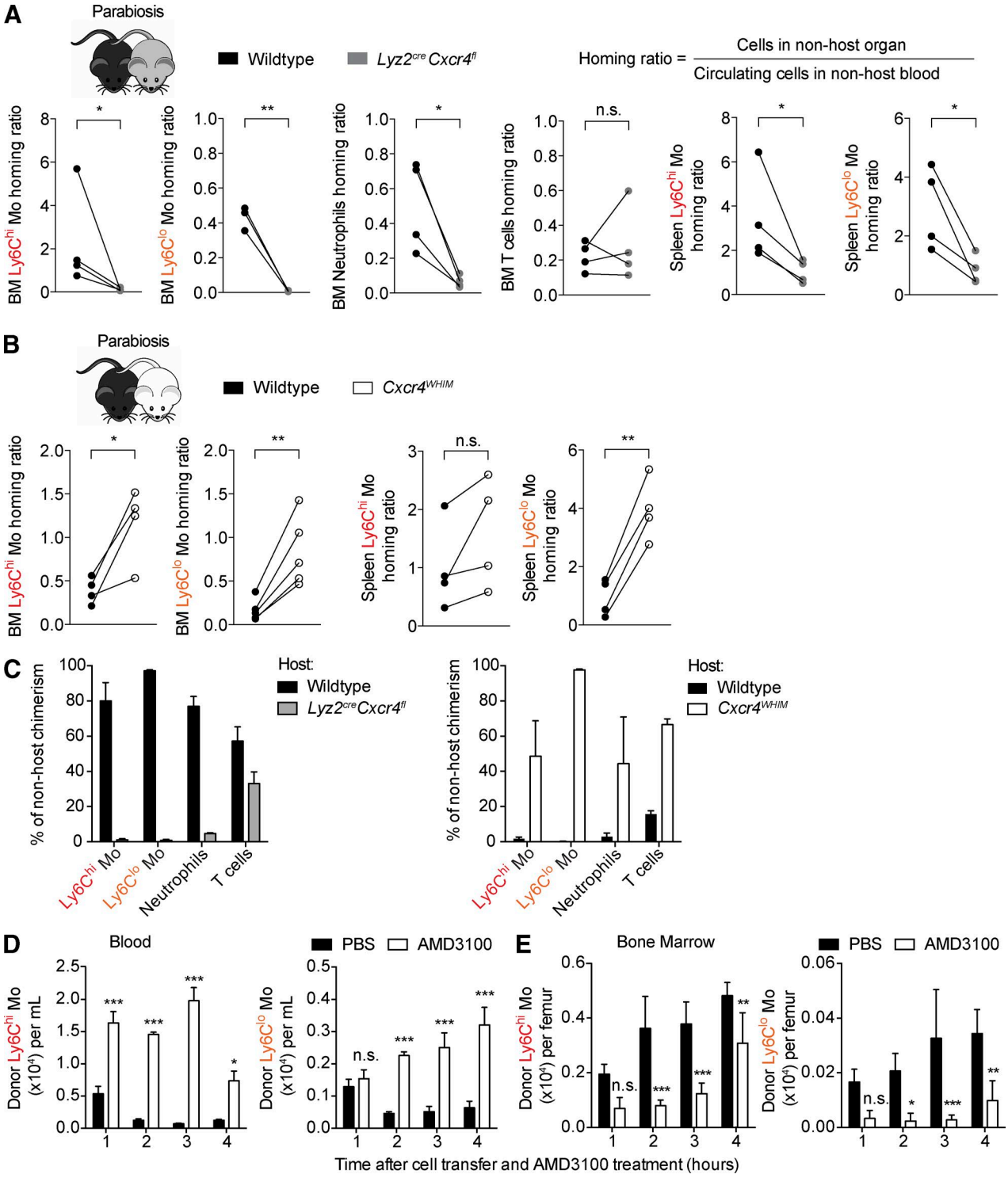

Figure 6. **CXCR4 regulates homing of monocytes back to reservoirs.** (A and B) Homing capacity (calculated as a ratio) of monocytes or indicated immune cells of WT and *Lyz2*^{cre}*Cxcr4*^{fl} (A) or *Cxcr4*^{WHIM} (B) into the BM or spleen of their respective partners in parabiotic mice. Monocyte, neutrophil and T cell numbers were quantified in blood, BM and spleen before calculation of the respective homing ratios to normalize for unequal exchange in circulating leukocytes (n = 4–5). ns, not significant; *, $P < 0.05$; **, $P < 0.01$ (Student's t test). Results are representative of one out of two independent experiments. (C) Percentage of nonhost cells present in blood of WT and *Lyz2*^{cre}*Cxcr4*^{fl} mice (left), and WT and *Cxcr4*^{WHIM} parabiotic mice (right). Results are expressed as

more, Ly6C^{hi} monocytes did not accumulate in the lungs of *Lyz2^{cre}Cxcr4^{fl}* mice in a high-grade cecal ligation and puncture (CLP) model of sepsis (Fig. 9 G) and exhibited a significant improved survival outcome compared with *Cxcr4^{fl}* control mice (Fig. 9 H). Together, these data suggest that CXCR4 continues to play important roles in regulating monocyte margination in the pulmonary circulation, whereas disruption of its signaling ameliorated lung injury and sepsis mortality.

DISCUSSION

In this study, we report the discovery of heterogeneity among BM Ly6C^{hi} monocytes. Specifically, BM Ly6C^{hi} monocytes consist of two developmentally related subsets of monocytes (CXCR4^{hi} and CXCR4^{lo} subpopulations) that are functionally distinct in their immunological roles. Furthermore, we extend the role of CXCR4 beyond its reported function as a mere BM anchoring signal by demonstrating its involvement in the control of monocyte tissue trafficking activities. Specifically, we reveal that CXCR4 controls monocyte margination in the lung vasculature and contributes to lung injury and sepsis-induced mortality. Our study hence provides a conceptual advancement in the understanding of monocyte biology by identifying the presence of a transitional precursor population among BM Ly6C^{hi} monocytes and deciphering the peripheral mechanisms that control monocyte homeostasis in the tissue (Fig. 10).

Using a combination of computational analytical approaches and flow cytometric analysis, we observed that cMoP-derived BM Ly6C^{hi} monocytes consist of two distinct subpopulations defined by CXCR4 expression. Isolation of these cells revealed that CXCR4^{hi} and CXCR4^{lo} subpopulations are transcriptionally distinct. In particular, the CXCR4^{hi} subpopulation was enriched in genes associated with cell cycle, cell division, and DNA repair whereas the CXCR4^{lo} subpopulation was over-represented with genes associated with cellular activation, phagocytosis, motility, and pattern recognition. Comparative analysis of the CXCR4^{hi} subpopulation with its progenitor, cMoP, also revealed distinct genetic differences, with the CXCR4^{hi} subset displaying a more mature phenotype than cMoPs. Our results hence suggest that a considerable amount of functional maturation continues to occur in the CXCR4^{hi} subpopulation. Consistent with this notion, results from our functional studies validated that the CXCR4^{hi} subpopulation is actively proliferating and displayed reduced bead internalization in vivo compared with the CXCR4^{lo} subpopulation. More importantly, we show that the CXCR4^{hi} subpopulation gives rise to mature CXCR4^{lo} Ly6C^{hi} monocytes over time. Furthermore, this CXCR4^{hi} subpopulation, like cMoPs, remains immobilized in the BM even under inflammatory conditions and is insensitive toward circadian rhythmic fluctuations. Together, we propose that the CXCR4^{hi} subpopulation of BM Ly6C^{hi} monocytes represents a population of transitional premonocytes (TpMo). It is noteworthy that although Hettinger et al. (2013) have shown the cMoP to be the only subset in the BM monocyte fraction to form colonies and is committed strictly toward monocyte development, it remains unclear if cMoPs are fully committed toward the Ly6C^{hi} monocyte lineage, or may give rise to Ly6C^{lo} monocytes independent of their differentiation from Ly6C^{hi} monocytes (Thomas et al., 2015). Because our CMap analysis and in vivo data strongly demonstrates a linear development of Ly6C^{hi} monocytes from TpMo, it is likely that the loss of c-kit on TpMo represents a loss of self-renewal ability (Ogawa et al., 1991) upon their differentiation from cMoPs, and that TpMos differ from cMoPs by serving as the first fully committed and immediate precursor of mature Ly-6C^{hi} monocytes. More importantly, we believe that this newly defined developmental transition forms a regulatory checkpoint that prevents an uncontrolled release and allows for the rapid replenishment of BM monocytes. Our results also suggest a new working model whereby monocytes program their intrinsic mobilizing capacity according to their functional maturity, which ensures that only functionally mature monocytes are being mobilized into the circulation.

It is well established that CXCR4-signaling plays a critical role in multiple biological processes in the BM compartment (Nagasawa, 2014). Consequently, studies have implicated a role for CXCR4 in monocyte retention in the BM (Jung et al., 2015; Liu et al., 2015). However, it remains unclear if reduced expression of CXCR4 on monocytes, upon their exit from the BM, indicates its diminished role in monocyte biology in the circulation. Contrary to this assumption, we observed that CXCR4 functions as an important mediator in the spatiotemporal localization of monocytes in peripheral compartments. Notably, monocytes have been shown to shuttle back to the BM through an unknown mechanism (Varol et al., 2007). Using parabiosis and adoptive transfer approaches, we provide the first experimental evidence of CXCR4-mediated BM homing as a key mechanism in regulating circulating monocyte numbers, which is in line with postulations discussed by Wang et al. (2009). Furthermore, we found a similar trend in CXCR4-dependent homing into the spleen, which further supports the idea that the spleen contains a reservoir of bona fide monocytes (Swirski et al., 2009) that is not simply synonymous with the blood pool. Although we believe that the BM remains the major compartment where circulating monocytes home to as the spleen reservoir (Swirski et al., 2009) and its CXCL12 expression (Inra et al., 2015) are much smaller than that of the BM, splenic monocytes are mobilized during vascular and ischemic injury

mean ± SD (n = 4–5) and representative of one out of two independent experiments. (D and E) Total number of donor (CD45.1$^+$) monocytes with a Ly6C^{hi} (left) or Ly6C^{lo} (right) phenotype detected in blood (D) or BM (E) in recipient CD45.2$^+$ mice that had been pretreated with or without AMD3100. Results are expressed as mean ± SD (n = 4) and representative of one out of three independent experiments. *, $P < 0.05$; **, $P < 0.01$; ***, $P < 0.001$ (two-way ANOVA).

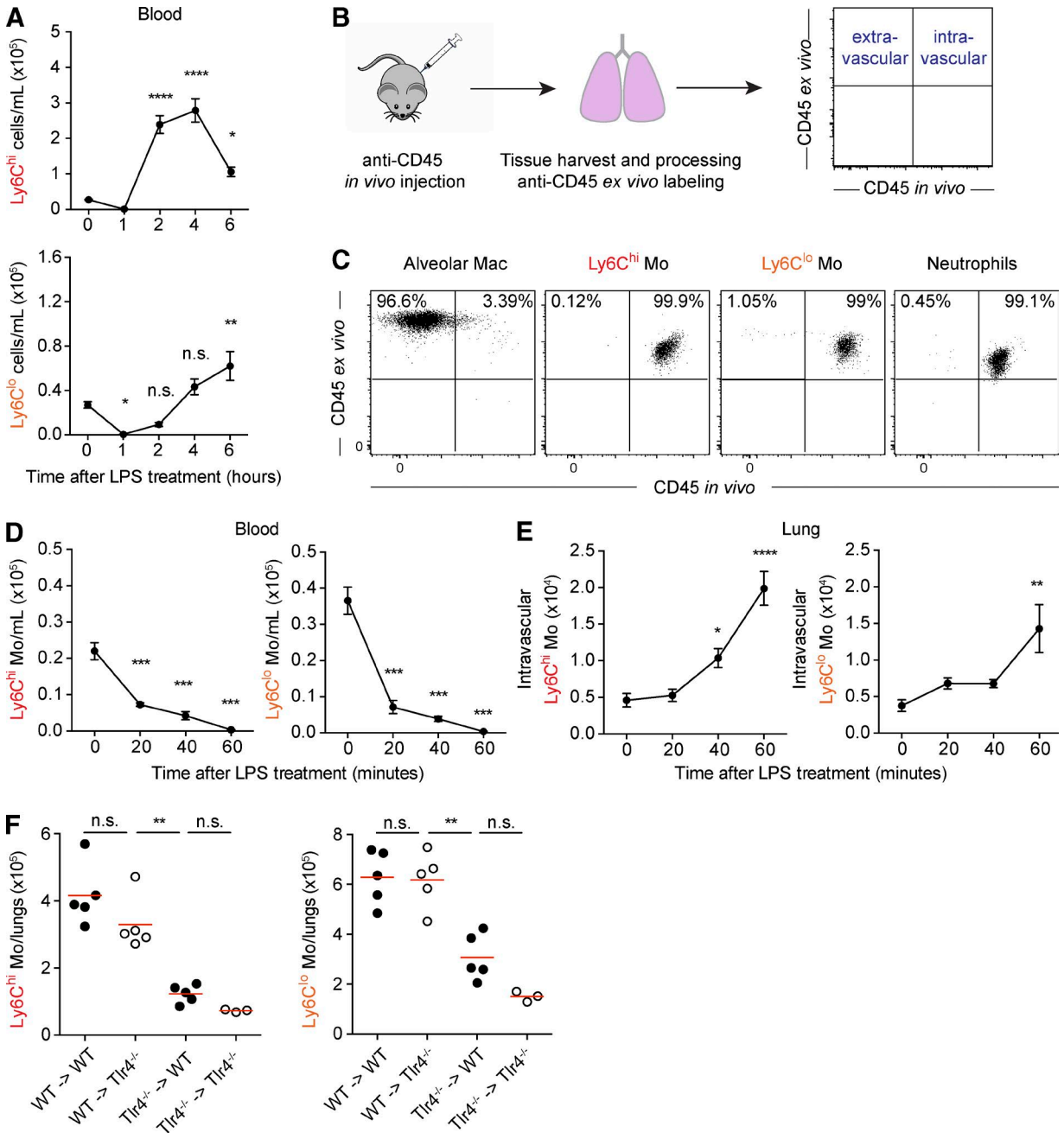

Figure 7. **Endotoxemia promotes monocyte retention in the pulmonary circulation.** (A) Blood Ly6C^{hi} (top) and Ly6C^{lo} (bottom) monocyte counts after i.v. treatment with 10 ng LPS. Results are expressed as mean ± SEM (n = 4) and representative of one out of three independent experiments. ns, not significant; *, P < 0.05; **, P < 0.01; ****, P < 0.0001 (one-way ANOVA). (B) Illustration showing the intravascular labeling of leukocytes with anti-CD45 antibodies. (C) Representative flow cytometry plots showing the extravascular and intravascular localization of lung immune cells of one out of three independent experiments. (D and E) Quantification of Ly6C^{hi} (left) and Ly6C^{lo} (right) monocytes in blood (D) and lung tissues (E) from LPS-treated mice. Results are expressed as mean ± SEM (n = 4) and representative of one out of four experiments. ns, not significant; *, P < 0.05; **, P < 0.01; ***, P < 0.001; ****, P < 0.0001 (one-way ANOVA). (F) WT and *Tlr4*$^{-/-}$ chimeric mice were analyzed for Ly6C^{hi} monocyte numbers after 1 h of LPS administration. Each data point represents one individual mouse and results are representative of two individual experiments. ns, not significant; **, P < 0.01 (one-way ANOVA).

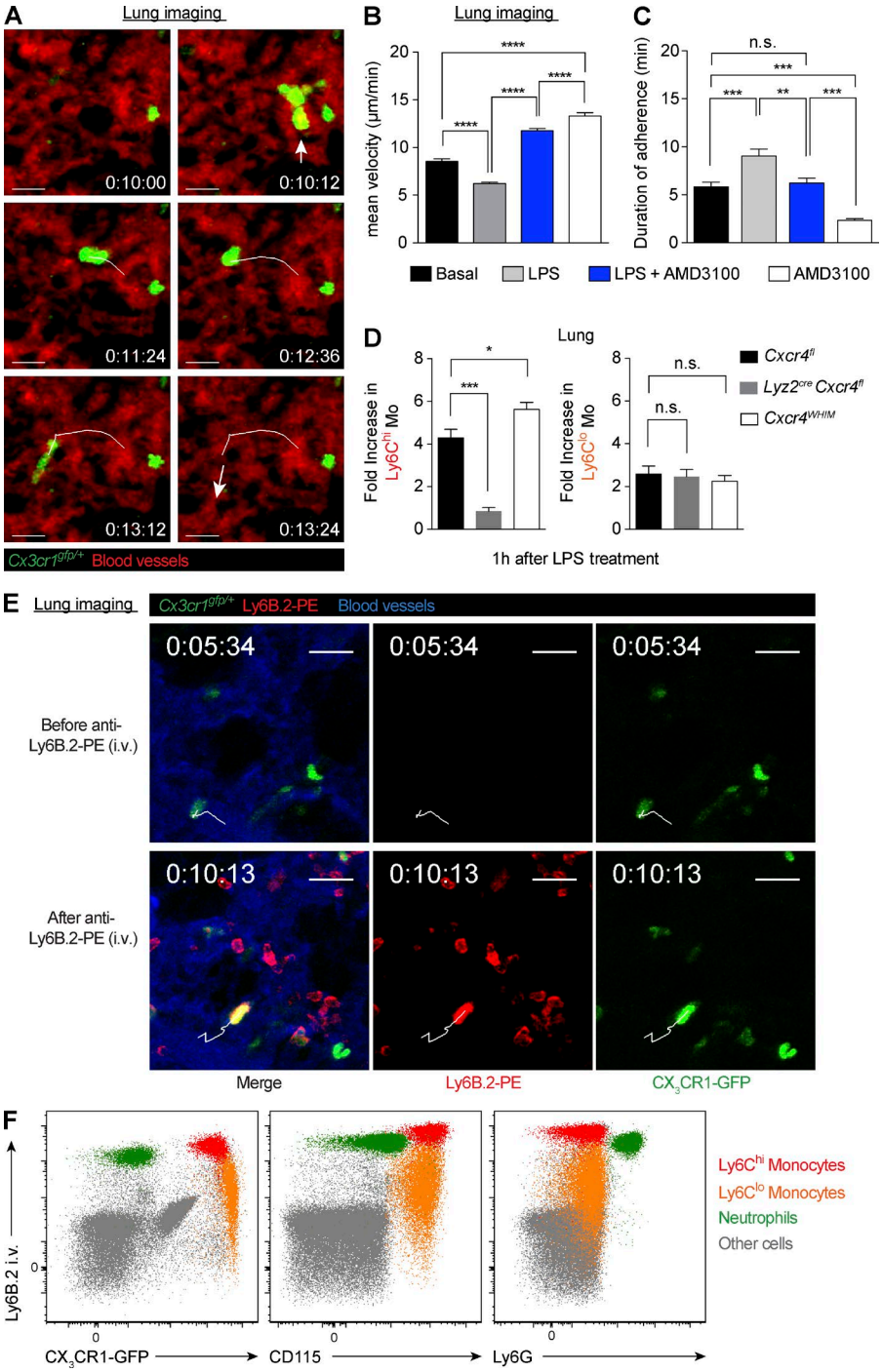

Figure 8. **Monocytes marginate in the pulmonary vasculature.** (A) A representative GFP$^+$ monocyte (arrowhead) alters its morphology through pulmonary capillaries. Bar, 15 µm (time, h:mm:ss; green, CX$_3$CR1$^+$ cells; red, TRITC-dextran). Results are representative of one out of three independent experiments. (B and C) Monocyte mean velocity (B) and duration of adherence (C) after indicated treatments. Results are pooled from three independent experiments per treatment and are expressed as mean ± SEM. ns, not significant; **, P < 0.01; ***, P < 0.001; **** P < 0.0001 (one-way ANOVA). (D) LPS-induced fold-increase in lung Ly6C^{hi} (left) and Ly6C^{lo} (right) monocytes 1 h after treatment. Results expressed as mean ± SEM (n = 4–7). ns, not significant; *, P < 0.05; ***, P < 0.001 (one-way ANOVA). (E) Snapshots of GFP$^+$ monocytes in the lung of a *Cx3cr1*$^{gfp/+}$ reporter mouse, before (top) and after (bottom) i.v. administration of a Ly6B.2-PE antibody (4 µg). A representative GFP$^+$ monocyte is depicted migrating through pulmonary capillaries (white track), becomes PE$^+$ after antibody administration Bar, 15 µm (time, h:mm:ss; green, CX3CR1$^+$ cells; red, Ly6B.2$^+$ cells; blue, Evans blue). Results are representative of one out of three independent experiments. (F) FACS plots of lungs from *Cx3cr1*$^{gfp/+}$ mice i.v. injected with Ly6B.2-PE. Ly6C^{hi} (red), Ly6C^{lo} monocytes (orange), and neutrophils (green) were plotted in relation to Ly6B.2 expression. Results are representative of one out of three independent experiments.

and increase in numbers through extramedullary hematopoiesis (Leuschner et al., 2012; Robbins et al., 2012). Therefore, future work would be required to determine the extent of monocyte homing to the spleen in these scenarios.

Leukocytes rely heavily on the circulatory system to transport themselves to various tissues/organs. During this trafficking process, leukocytes may interact with endothelial cells for prolonged periods of time, which determines their transit time in organs. However, the functional outcomes of these leukocyte intravascular activities have been underappreciated. It has been proposed that the marginated pool is caused by the need for leukocytes to alter their morphology as they transit and crawl through small-caliber microvessels (Kuebler and Goetz, 2002). In particular, the lung represents a major site of leukocyte margination (Staub and Schultz, 1968; Hogg, 1987) and is the only organ to receive the full

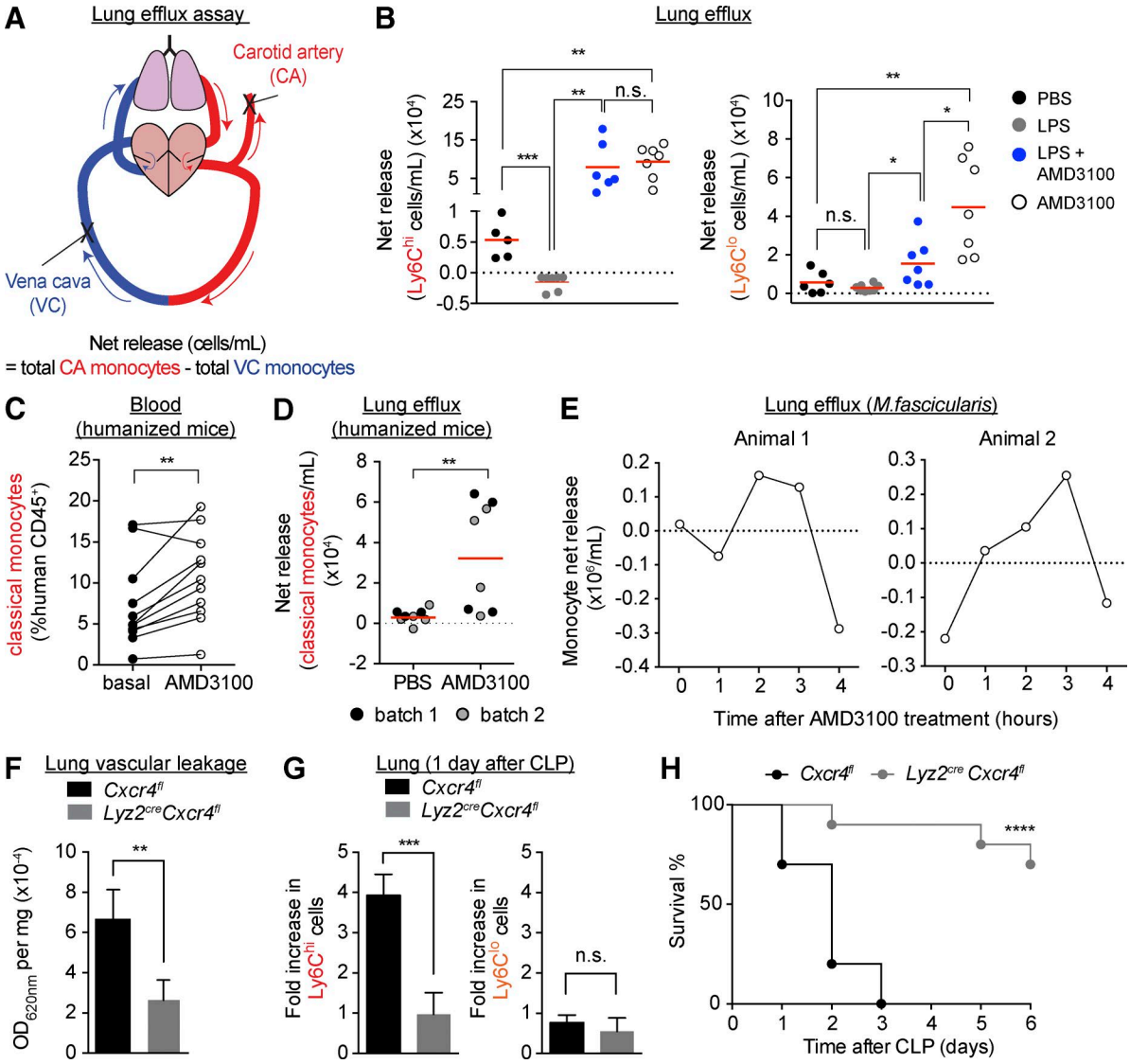

Figure 9. **CXCR4 regulates pulmonary monocyte margination and predisposition to injury.** (A) Schematic of the lung efflux assay. (B) Monocyte numbers released from the lung vasculature after indicated treatments. Results expressed as mean (n = 5–7 per group) and representative of one out of three independent experiments. ns, not significant; *, P < 0.05; **, P < 0.01; ***, P < 0.001 (one-way ANOVA). (C and D) Frequency of blood (C) and pulmonary release (D) of $CD14^+CD16^-$ classical monocytes in humanized mice at baseline and 2 h after AMD3100 treatment (n = 8–11). Results are representative of one out of two independent experiments. **, P < 0.01 (Student's t test). (E) Net monocyte release from the lungs of two individual nonhuman primates (*Macaca fascicularis*) over a 4-h observation period. (F–H) *Lyz2*^{cre}*Cxcr4*^{fl} mice were compared with *Cxcr4*^{fl} control mice for lung vascular leakage during acute lung injury (F; n = 5; **, P < 0.01, Student's t test) or fold-increase accumulation of lung $Ly6C^{hi}$ (left) and $Ly6C^{lo}$ (right) monocytes (G; n = 3–5; ***, P < 0.001, Student's t test) and their mortality using the Kaplan-Meier survival curve (H; n = 10; ****, P < 0.0001, Mantel-Cox) in the CLP sepsis model. Results are representative of one out of three independent experiments.

cardiac output. Previous studies have shown that leukocyte margination depends on a balance between the propelling force executed by the shear stress of blood flow (Martin et al., 1982) and a retaining force that delays monocyte transit. Data from our intravital imaging and lung efflux experiments suggest that CXCR4 interactions partly constitute the retention force in the lung vasculature. Importantly, we were able to successfully replicate these findings in both humanized mice and in a nonhuman primate model, suggesting that CXCR4 regulation of monocyte margination is likely to be physiologically relevant in humans.

Although leukocyte margination is a fundamental physiological process, their dysregulated intravascular migration and uncontrolled aggregation are associated with several human inflammatory diseases (MacNee and Selby, 1993; Looney and Bhattacharya, 2014). Here, we show that LPS

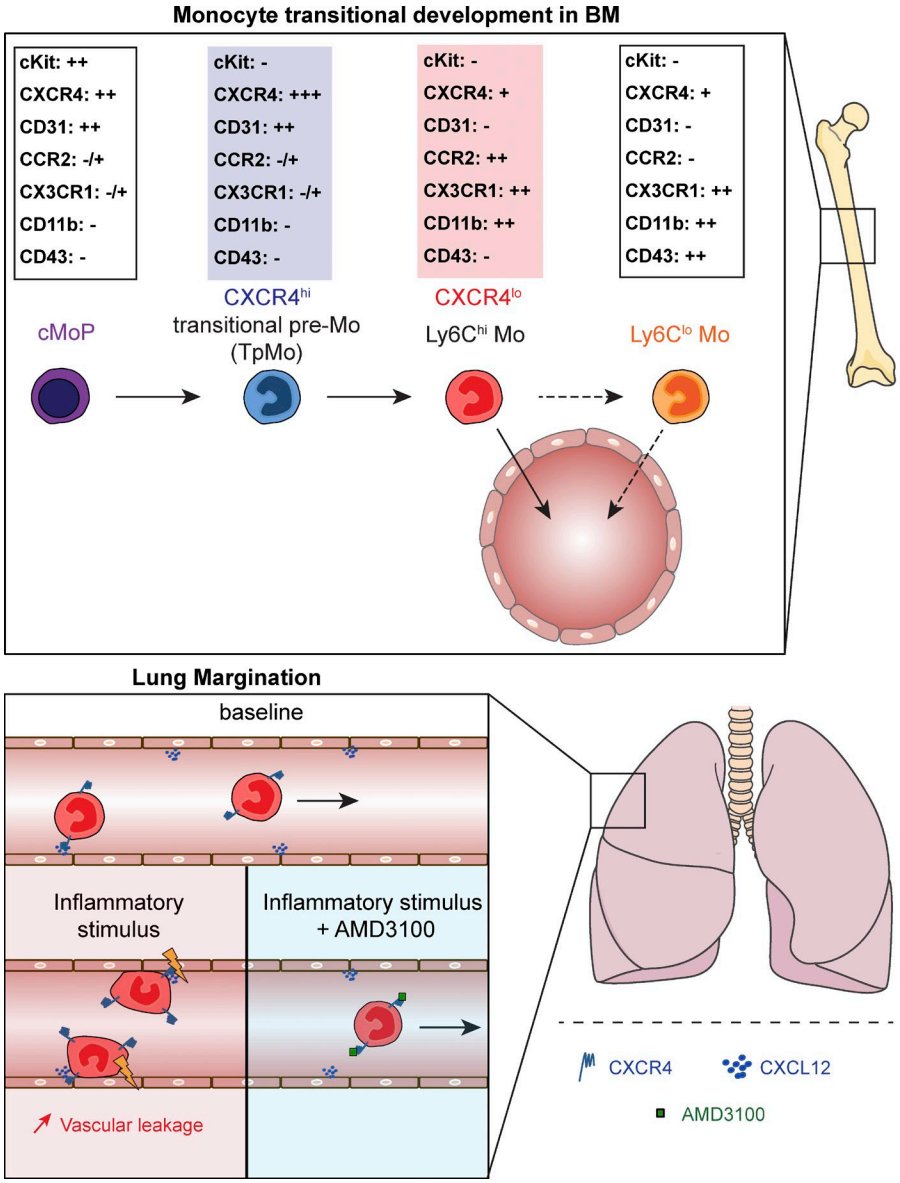

Figure 10. **CXCR4 identifies a TpMo population in the BM and mediates monocyte cellular responses in peripheral tissues.** (top) Monocytes arise from cMoPs and undergo a developmental pathway that ends with Ly6C^{lo} monocytes as the terminally differentiated form of monocytes. In this study, we propose that cMoP-differentiated Ly6C^{hi} monocytes undergo a developmental transition, which involves a transitional premonocyte (TpMo) stage, before giving rise to mature Ly6C^{hi} monocytes. TpMos are identified based on their CXCR4^{hi} expression compared with mature Ly6C^{hi} monocytes that are CXCR4^{lo}. Furthermore, TpMos can be distinguished from cMoPs based on their negative expression for c-kit. Functionally, TpMos are immobilized in the BM to serve as an immediate precursor for the active pool of mature CXCR4^{lo} Ly6C^{hi} monocytes. (Bottom) Upon entering the circulation, CXCR4 plays a significant role in monocyte margination in the pulmonary vasculature. Exposure to subclinical LPS doses triggers increased pulmonary monocyte margination, leading to a transient state of monocytopenia that can be reversed with CXCR4 inhibition using AMD3100. Disruption in CXCR4 signaling also attenuated lung injury and prevented sepsis mortality.

triggers increased pulmonary accumulation of inflammatory Ly6C^{hi} monocytes that leads to lung injury but is ameliorated by CXCR4 inhibition. On the other hand, it appeared that CXCR4 did not play a significant role in Ly6C^{lo} monocyte margination during endotoxemia, suggesting that Ly6C^{lo} monocytes may use a different array of molecules to interact with the endothelium, such as integrins, as supported by a previous study (Carlin et al., 2013). Nevertheless, our study provides a mechanistic understanding of how CXCR4 antagonism may attenuate lung inflammatory diseases, as described by previous studies (Lukacs et al., 2002; Drummond et al., 2015). Furthermore, we show that interfering with CXCR4 signaling results in reduced monocyte accumulation in the lung, which was associated with increased sepsis survival. Notably, although monocytes are essential for bacteria clearance, they are also major contributors of the cytokine storm that leads to organ damage and mortality (Weber et al., 2015). Furthermore, monocyte depletion during ALI has been shown to improve the outcome of vascular injury (O'Dea et al., 2009; Dhaliwal et al., 2012). However, it is important to note that more experimental work would be required to determine the immune and organ-specific contexture of monocyte margination in the lung. Hence, our study shows that CXCR4-mediated monocyte compartmentalization may serve as a major biological regulatory mechanism that underlies immune homeostasis to prevent excessive damage to the host.

In summary, our study provides new insight into the current framework of monocyte development and homeostasis by identifying a previously undescribed population of TpMo among BM Ly6C^{hi} monocytes. Furthermore, our results extend the role of CXCR4 beyond its function as a BM retentive force to an important regulator in the peripheral

tissue compartment with implications in pulmonary inflammation. Hence, we envision that our results will provide a new framework for understanding monocyte biology and may lead to the engineering of improved monocyte-targeting therapeutic strategies.

MATERIALS AND METHODS

Mice and treatments

C57BL/6 mice (6–10-wk-old) were bred and maintained under specific pathogen–free conditions in the Biological Resource Centre (BRC) of A*STAR, Singapore. *Lyz2*$^{cre/cre}$ (B6.129P2-*Lyz2*$^{tm1(cre)Ifo}$/J), *Cx3cr1*$^{gfp/+}$ (B6.129P-*Cx3cr1*^{tm1Litt}/J), *Cxcr4*$^{fl/fl}$ (B6.129P2-*Cxcr4*^{tm2Yzo}/J), NOD-*scid Il2rg*$^{-/-}$ (NSG; NOD.Cg-*Prkdc*^{scid} *Il2rg*^{tm1Wjl}/*SzJ*), *Rosa26*$^{mT/mG}$ (STOCK *Gt(ROSA)26Sor*$^{tm4(ACTB-tdTomato,-EGFP)Luo}$/J), and CD45.1 mice were obtained from The Jackson Laboratory. Fucci-474 mice were from the Institute of Physical and Chemical Research BioResource Center (Ibaraki, Japan; Sakaue-Sawano et al., 2013). *Lyz2*$^{cre/cre}$ mice were crossbred in-house with *Cxcr4*$^{fl/fl}$ mice to generate progeny that were CXCR4-deficient in the myeloid lineage only (termed *Lyz2*^{cre}*Cxcr4*^{fl}; Eash et al., 2009). *Tlr4*$^{-/-}$ mice were obtained from Oriental BioService. Gain-of-function *Cxcr4*$^{1013/+}$ mice (termed *Cxcr4*^{WHIM}) were provided by F. Bachelerie (Balabanian et al., 2012). For fate-mapping purposes, *Lyz*^{cre}*Cxcr4*^{fl} were crossed to *Rosa26*$^{mT/mG}$ mice (termed *Rosa*$^{mT/mG}$*:Lyz*^{cre}*Cxcr4*^{fl}). Humanized mice were generated as described (Chen et al., 2013). All transgenic mice were maintained on a C57BL/6 background and experiments were performed under the approval of the Institutional Animal Care and Use Committee (IACUC) of the BRC, in accordance with the guidelines of the Agri-Food and Veterinary Authority (AVA) and the National Advisory Committee for Laboratory Animal Research (NACLAR) of Singapore. Mice were treated with 5mg/kg AMD3100 (plerixafor; Sigma-Aldrich) via subcutaneous injection and/or with 10 ng LPS derived from *Escherichia coli* (serotype O55:B5; Alexis Biochemicals) administered via intravenous route. All experiments were performed between ZT4 to ZT8 unless otherwise stated.

Tissue preparation for flow cytometry and sorting

Blood was obtained via cardiac puncture or incision in the submandibular region and was then treated with commercial-grade red blood cell lysis buffer (eBioscience). Lungs were removed en bloc in experiments looking at pulmonary margination and mice were perfused with PBS containing 2 mM EDTA using a peristaltic pump (MINIPULS 3; Gilson), followed by removal of the spleen and femurs. Lungs and spleens were finely minced and homogenized to single-cell suspensions using 70-µm nylon mesh sieves with syringe plungers (O'Dea et al., 2009). Mice femurs were flushed and the effluent passed through a 70-µm nylon mesh sieve to obtain a BM cell suspension. Human BM mononuclear cells were purchased from Lonza and processed according to the manufacturer's instructions. Antibodies were purchased from eBioscience, BioLegend, BD, or R&D Systems. Mouse cells were stained with the following antibodies: CCR2 (475301), CD3e (145-2C11), CD4 (GK1.5), CD8 (53–6.7), CD11b (M1/70), CD11c (N418), CD16/32 (93), CD19 (eBio1D3), CD31 (390), CD34 (RAM34), CD43 (S7), CD45 (30-F11), CD45.1 (A20), CD45.2 (104), CD45R/B220 (RA3-6B2), CD49a (HMα1), CD49f (GoH3), CD62L (MEL-14), CD71 (YTA74.4), CD88 (20/70), CD115 (AFS598), CD172a (P84), CD274 (10F.9G2), cKit (2B8), CXCR4 (2B11), CX3CR1 (SA011F11), F4/80 (CI:A3-1), Flt3 (A2F10), IA-IE (M5/114.152), Ly6C (HK1.4), Ly6G (1A8), NK1.1 (PK136), and Ter119 (TER-119). Human cells were stained with the following antibodies: CD3 (UCHT1), CD10 (eBioCB-CALLA), CD11b (ICRF44), CD11c (B-ly6), CD14 (322A-1), CD16 (3G8), CD19 (HIB19), CD20 (2H7), CD34 (581), CD45 (HI30), CD56 (MEM188), CD123 (6H6), CXCR4 (12G5), and HLA-DR (L243). Dead cells were identified and excluded using DAPI staining. Lung, blood, and BM monocytes were identified as CD45$^+$CD115$^+$cKit$^-$Ly6G$^-$Lineage (CD3, CD19, CD45R, and NK1.1) negative and Ly6C^{hi}CD43$^-$ or Ly6C^{lo}CD43$^+$ according to the subset in mice and human BM classical monocytes identified as CD14$^+$CD16$^-$CD11b$^+$CD34$^-$HLA-DR$^+$Lineage$^-$ (CD3, CD10, CD19, CD20, CD56, and CD123). Cells were acquired on a BD LSR II flow cytometer (BD) using FACSDiva Software, and data were analyzed using FlowJo Software (Tree Star). Total number of cells collected from blood or each tissue/organ was quantified using count beads (CountBright; Life Technologies) according to the manufacturer's protocol. CXCR4 expression on monocytes was quantified as median fluorescent intensity (MFI) and normalized by subtracting the fluorescence minus one (FMO) control. For cell sorting, BM cells were sorted using a FAC SAria II (BD) to achieve >98% purity.

BrdU pulsing and proliferation assays

For in vivo assays, mice were administered 1.5 mg BrdU (BD) via intraperitoneal injection at indicated time points for cell tracking or for 30 min to assess their proliferative capacity. For in vitro cell proliferative assays, human BM cells were pulsed with 10 µM of BrdU for 45 min. To detect BrdU incorporation into monocytes, cells were surface-stained, fixed, permeabilized, and subjected to intracellular staining with FITC-conjugated anti-BrdU antibody, together with 7-AAD for cell cycle analysis, according to the manufacturer's protocol (BrdU Flow kit; BD) before analysis by flow cytometry. The Fucci transgenic mouse model, in which cells in the S/G2/M phase of the cell cycle were labeled with a green-emitting fluorescent protein, was also used to identify proliferating cells through flow cytometry.

In vivo bead uptake

The ability of cells to uptake beads in vivo was assessed as previously described (Tacke et al., 2007). In brief, 0.5 µm Fluoresbrite polychromatic red microspheres (2.5% solids

[wt/vol]; Polysciences Inc.) were diluted 1:25 in PBS, and 250 µl of the solution was injected into the lateral tail vein of mice. After 4 h, mice were sacrificed and BM was collected, flushed, and stained with antibodies to distinguish the different monocyte cell populations.

Adoptive transfer of BM monocytes

Femurs and tibias were harvested from CD45.1 mice and flushed with ∼5 ml PBS containing 3% FCS. RBCs were lysed and the remaining cells were resuspended in sterile PBS. A total of 10 million CD45.1 donor cells were adoptively transferred into CD45.2 recipient mice that were simultaneously treated with AMD3100 or PBS. Recipient mice were euthanized at the time points indicated in the respective figures, and the perfused femurs were harvested for flow cytometric identification of donor monocyte (CD45.1) sequestration into the BM of recipient animals (CD45.2). For intrafemoral transfer of BM Ly6C^{hi} monocyte subsets, sorted 5 × 10^5 CD45.1$^+$ CXCR4^{hi} were suspended in PBS and were transferred into the left femur of CD45.2$^+$ mice via an insulin syringe with a short needle (BD). At 8 and 24 h after cell transfer, BM femurs were collected, and the resulting cell suspensions were analyzed by flow cytometry to establish the phenotype of the CD45.1$^+$ progeny of the transferred cell populations.

Dimensionality reduction using t-SNE and automatic clustering

BM Ly6C^{hi} monocytes were manually gated from multicolor flow cytometry data. as shown in Fig. 1 A, and were exported in a FCS file. In this study, t-Distributed Stochastic Neighbor Embedding (t-SNE) dimensionality reduction was performed using bh_tsne, an implementation of t-SNE via Barnes-Hut approximations. R was used as an interface to execute bh_tsne, as previously described (Becher et al., 2014). K-means automatic clustering was performed using CYT in Matlab. 90,000 events were used for t-SNE dimensionality reduction.

Transcriptomics

cMoP, Ly6C^{hi}CXCR4^{hi}, Ly6C^{hi}CXCR4^{lo}, and Ly6C^{lo} monocytes were sorted according to the gating strategy shown in Fig. 2 A. After sorting, cells were incubated for 3 h in RPMI + 10% FCS and were then subjected to RNA isolation. Total RNA was extracted using Arcturus PicoPure RNA Isolation kit according to the manufacturer's protocol. All mouse RNAs were analyzed on Perkin Elmer Labchip GX system for quality assessment with RIN > 7.9. cDNA libraries were prepared using 2 ng of total RNA and 1 µl of a 1:50,000 dilution of ERCC RNA Spike in Controls (Ambion) using SMARTSeq v2 protocol (Picelli et al., 2014), except for the following modifications: (1) use of 20 µM TSO; and (2) use of 250 pg of cDNA with 1/5 reaction of Illumina Nextera XT kit. The length distribution of the cDNA libraries was monitored using DNA High Sensitivity Reagent kit on the Perkin Elmer Labchip. All eight samples were subjected to an indexed PE sequencing run of 2 × 51 cycles on an Illumina HiSeq 2500 Rapid mode (14 samples/lane).

RNA-Seq data in the form of FASTQ files were subsequently mapped to the mouse genome build mm10 using the STAR alignment software. The mapped reads were then counted using featureCounts (part of Subread package) based on the GENCODE M9 annotations. The raw counts were then used for a differential gene expression analysis (DEG) using edgeR (R version 3.1.2) with adjusted $P < 0.05$ and fold change >2 to identify genes differentially regulated in monocyte subsets. A filter for genes having a mean count of at least 10 was done to eliminate low expressing and non-expressing genes before DEG analysis. PCA of samples was done using $\log_2$CPM (count per million reads) values of all detected genes. PCA, volcano plot, and heat maps were done in R version 3.1.2. Pathway analysis of DEGs was done using IPA software (Qiagen).

Computational inference of developmental path

CMap (Lamb et al., 2006) analysis was performed using DEGs between Ly6C^{hi}CXCR4^{lo} and Ly6C^{lo} monocytes. Positive CMap scores indicate enrichment of Ly6C^{lo} signature genes, whereas negative CMap scores indicate enrichment of Ly6C^{hi} signature genes. R package seriation (Hahsler et al., 2008) was used to find a suitable linear order for cMoP, CXCR4^{hi}, and CXCR4^{lo} Ly6C^{hi} monocytes. Six different seriation methods, including TSP, R2E, ARSA, HC, GW, and OLO, were applied. TSP, ARSA, and OLO produced the best and identical results with regard to the shortest path length, minimal AR events, and minimum Moore stress. Seriation analysis was done using $\log_2$CPM values of all detected genes. PCA, CMap, and seriation analyses suggest a developmental path from cMoP to CXCR4^{hi}, followed by CXCR4^{lo} Ly6C^{hi} monocyte.

Wanderlust was executed using CYT in Matlab, as previously described (Bendall et al., 2014). Wanderlust was run on six phenotypic markers: CXCR4, CD31, CD16/32, CX_3CR1, CCR2, and CD11b, using the following parameters: number of neighbors l = 30, k = 5, number of landmarks nl = 20, number of graphs to generate ng = 25, distance metric = angular. The starting point (early events) consisted of selected Ly6C^{hi} cells that expressed high levels of CXCR4, CD31, and CD16/32, as observed on cMoPs, which is the most direct progenitor of BM Ly6C^{hi} monocytes. 90,000 events were used for Wanderlust analysis.

Parabiosis and BM chimeric mice

Female mice were anesthetized using 2.5% Avertin (15 ml/kg), shaved at the corresponding lateral sides of the body, and then surgically joined as previously described (Hashimoto et al., 2013). After surgery, the mice were treated with Baytril (0.05–2 mg/kg s.c.) and Buprenorphine (5–20 mg/kg s.c.) and allowed to recover for 8 wk. Since *Lyz2^{cre}Cxcr4^{fl}* and *Cxcr4^{WHIM}* mice exhibit steady-state monocytosis and monocytopenia, respectively, parabiosis with WT animals results in unequal exchange of circulating leukocytes (Fig. 6 C); the re-

sults of these experiments were hence represented as a homing ratio to control for differences in absolute cell numbers between these mice. To determine the number of cells that had infiltrated a given organ, the number of nonhost cells present in that organ was divided by the total number of nonhost cells present in the host circulation (expressed as the homing ratio). To determine the total number of circulating cells, the blood volume present in an individual mouse was calculated using the formula: $y = 0.0715\ x$, where y and x represent the blood volume (milliliters) and body weight (grams), respectively, as previously described (van Furth and Sluiter, 1986).

To generate BM chimeric mice, 6-wk-old WT and *Tlr4*$^{-/-}$ mice were irradiated with two doses of 550 rad spaced 3 h apart and reconstituted with BM from WT or *Tlr4*$^{-/-}$ mice under sterile conditions. Recipient mice were analyzed 6 wk after irradiation, and number of Ly6C^{hi} monocytes were quantified 1 h after administration of LPS.

Scanning electron microscopy

Sorted CXCR4^{hi} and CXCR4^{lo} monocytes were seeded onto coverslips and incubated at 37°C, 5% CO_2, for 3 h to allow cell adhesion onto coverslips. Cells were fixed with 2.5% Glutaraldehyde (Sigma-Aldrich) in PBS, washed, and post-fixed in 1% Osmium tetroxide (Electron Microscopy Services) in PBS, and then dehydrated in ethanol and processed by critical point drying (EM CPD030; Leica). Finally, samples were sputter-coated with gold using an EM SCD050 (Leica) and imaged on the JSM-6701F, JEOL scanning electron microscope at 4,000 × magnification. 60–70 cells were acquired for each tested group and representative images of a typical phenotype were presented in the figure.

Intravital multiphoton imaging of lung

Imaging of the lung was performed as previously described (Looney et al., 2011). In brief, mice were anaesthetized with a cocktail of ketamine and xylazine before cannulation of the trachea to allow connection to a mechanical ventilator (tidal volume, ∼8–10 µl/g body weight; respiratory rate, ∼120 breaths per minute; MiniVent 845; Hugo Sachs Elektronik). Mice were then placed onto a heat pad to maintain body temperature at 37°C, followed by the removal of skin, muscle, and two rib bones to expose the lung. A custom-made vacuum window ring was used to immobilize the lung via application of a negative pressure vacuum (∼40 mmHg). To label the pulmonary vasculature, 70kD TRITC-conjugated dextran (250 µg in 100 µl saline; Sigma-Aldrich) or Evan's blue (50 µg in 50 µl sterile PBS) was administered i.v. into mice. Experimental groups consisted of mice administered with AMD3100 s.c., LPS i.v., or a combination of AMD3100 and LPS administered together via the different routes. Imaging of the lung began 45 min after single treatment with AMD3100 or LPS, whereas co-treatment of both AMD3100 and LPS were imaged at 2 h into AMD3100 and 45 min into LPS simultaneously. For the visualization of monocyte subsets, 4 µg of Ly6B.2-PE (Novus Biologicals) were administered i.v. in *Cx3cr1*$^{gfp/+}$ mice (Fig. 8, E and F). Experiments were performed at 880 or 990 nm excitation and 364 × 364 µm images were acquired in fast mode over a period of 30 min using a 4-µm z-step size with an approximate depth of 20 µm. After acquisition, images were averaged to match respiratory movements, and drifts during imaging were corrected where necessary (FIJI software). Images were subsequently transformed into time series movies using Imaris. Tracking of GFP$^+$ cells was performed semiautomatically using Imaris spot-tracking algorithms, and mean velocity was extracted. The duration of GFP$^+$ cell adherence in the lung vasculature was tabulated manually.

Localization of intravascular lung monocytes

Intravascular staining of lung monocytes was performed in vivo according to a previously described protocol (Anderson et al., 2014). In brief, mice were anaesthetized by isoflurane inhalation and APC-conjugated anti-CD45.2 (clone 104; eBioscience) was administered i.v. (4 µg antibody in 200 µl saline). The antibody was allowed to circulate for 3 min before the mice were euthanized. Lungs were removed en bloc and processed immediately in an excess volume of PBS containing 3% FCS and 2 mM EDTA to dilute any excess antibody. FITC-conjugated anti-CD45.2 (clone 104; eBioscience) was included in the antibody-staining panel to identify extravascular cells.

Lung efflux assay

The method used for tandem blood sample collection from the carotid artery and vena cava has been described previously (Devi et al., 2013). In brief, mice were anesthetized with isoflurane and a midline incision was performed on the neck to expose the underlying carotid artery. A microvascular clamp was applied to the artery, which was then cannulated by insertion of EDTA-filled polyethylene 10 tubing (inner diam, 0.28 mm; outer diam, 0.61 mm). After securing the cannula with a surgical suture, the clamp was released and ∼40 µl of arterial blood was collected into an Eppendorf tube. Blood was simultaneously drawn from the inferior vena cava using a 26-gauge needle attached to a prefilled EDTA syringe. Samples were collected 1 h after LPS injection, or 2 h after AMD3100 treatment. For mice that were cotreated with AMD3100 and LPS, the CXCR4 inhibitor was administered 1 h before injection of LPS, and blood sample collection took place an additional 1 h later. Both arterial and venous blood samples were subsequently analyzed by flow cytometry.

For lung efflux assays done on nonhuman primates, all experiments were performed on adult female *Macaca fascicularis* at the Singhealth Experimental Medicine Center (accredited by the Association for Assesment and Accrediation of Laboratory Animal Care) under approval #2012/SHS/692 from the Institutional Animal Care and Use Committee of Singapore, as previously described (Devi et al., 2013). In brief, midline laparotomy was performed under general anesthesia and ∼1 ml of blood was each collected from the abdominal

aorta and inferior vena cava at baseline and hourly intervals after s.c. administration of AMD3100 (0.5 mg/kg). Monocyte numbers were determined using a Hematology Analyzer (Beckman-Coulter).

The number of monocytes leaving the pulmonary circulation (termed net release) was calculated by subtracting the number of monocytes present in the venous blood sample from the number of monocytes present in the arterial blood sample.

Pulmonary vascular permeability assay

To assess the influence of monocytes or CXCR4-signaling on pulmonary vascular permeability, we used a LPS-Zymosan induced model of ALI (O'Dea et al., 2009). For the induction of ALI, mice were administered i.v. with 10 ng of LPS for 2 h. Subsequently, 150 µg in 100 µl of Zymosan-A (Sigma-Aldrich) was resuspended with 5 µl per g of 10 mg/ml of Evans blue (Sigma-Aldrich) and injected i.v. into mice. Mice were sacrificed 1 h later and lungs were perfused with PBS using a peristaltic pump (MINIPULS 3, Gilson). Lungs were weighed and Evans blue was extracted from the lung by incubating samples in 1 ml of N,N-dimethlyformamide (Sigma-Aldrich) at 37°C overnight. The supernatant was separated by centrifugation at 5,000 *g* for 30 min. The concentration of Evans blue in lung homogenate supernatants was quantified by a dual wavelength spectrophotometric method at absorptions of 620 and 740 nm, which allows for correction of contaminating heme pigments using the following formula: E_{620} (corrected) = $E_{620} - (1.426 \times E_{740} + 0.030)$

Chemotaxis assay

Femurs and tibias were harvested from C57BL/6 mice and flushed with ∼5 ml of PBS containing 3% FCS. RBCs were lysed and the resultant cells were suspended in sterile PBS for labeling with antibodies against CD11b, CD45, CD115, CXCR4, Flt3, cKit, and Ly6C, as well as an exclusion cocktail of antibodies against unwanted lineages (CD3, CD45R/B220, Ly6G, and NK1.1). BM monocytes were identified as $Lin^{-}Flt3^{-}cKit^{-}CD115^{+}Ly6C^{hi}$ cells that displayed either a $CXCR4^{hi}$ or $CXCR4^{lo}$ phenotype. The $CXCR4^{hi}$ and $CXCR4^{lo}$ subsets were then sorted at high speed using a BD FACSAria III apparatus (BD). A total of 10^5 sorted monocytes were transferred onto the top layer of a polycarbonate membrane with 3 µm pore size (Transwell; Corning), before being placed into lower chambers containing 0–50 ng of recombinant CCL2 (R&D Systems) and incubated at 37°C for 2 h. After incubation, the cells in the bottom chamber were harvested and analyzed by flow cytometry to determine the percentage of migrated monocytes (expressed as a proportion of the total cells that were initially loaded into the top chamber).

CLP-induced sepsis

Experimental procedures were performed as previously described (Rittirsch et al., 2009). In brief, the peritoneal cavity was exposed under ketamine/xylazine anesthesia and the cecum was exteriorized. ∼80% of the cecum was ligated distal of the ileo-cecal valve using a nonabsorbable 7–0 suture. A 23-gauge needle was used to perforate the distal end of the cecum, and a small drop of feces was extruded through the puncture before being relocated into the peritoneal cavity. The peritoneum was closed and subsequently treated with saline and Buprenorphine (5–20 mg/kg s.c.) via s.c. injection. Age-matched controls were included for all procedures.

Statistical analysis

Statistical analyses were performed using Prism software (GraphPad). Data were tested using either Student's *t* test (normal distribution) or ANOVA (one-way or two-way as appropriate), as indicated in the respective figure legends. $P < 0.05$ was considered significant.

Accession nos.

All RNA-sequencing data have been deposited at the National Center for Biotechnology Information Gene Expression Omnibus public database under accession no. GSE86079.

Online supplemental material

Fig. S1 shows heat maps of genes that are significantly and differentially expressed between cell subsets of the monocyte developmental pathway. Fig. S2 shows detailed histograms of cell surface marker expression for distinguishing monocyte subsets. Fig. S3 shows gating strategy for the analysis of CXCR4 expression on BM $Ly6C^{hi}$ monocytes. Fig. S4 shows gating strategy of blood monocytes in mice. Video 1 shows monocyte margination in the pulmonary vasculature. Video 2 shows the visualization of $Ly6C^{hi}$ monocytes in a *Cx3cr1*$^{gfp/+}$ mouse with an anti-Ly6B.2 antibody.

ACKNOWLEDGMENTS

We thank W.K. Chew and S. Chew for their technical help and support; the Singapore Immunology Network (SIgN) flow cytometry team for their assistance with cell sorting; Dr. Francesca Zolezzi and the SIgN functional genomics team for their assistance with transcriptomics; the SIgN mouse core facility for their mice expertise; Professor Toshio Suda and Dr. Norman Pavelka for their insightful scientific discussion and Dr. Neil McCarthy of Insight Editing London for his writing assistance.

This research was funded by SIgN, A*STAR, Singapore. C. Weber, J. Duchene, and M. Bianchini are supported by Deutsche Forschungsgemeinschaft (DFG) grant SFB1123-A1/Z1.

The authors declare no competing financial interests.

Submitted: 30 May 2016
Accepted: 1 September 2016

REFERENCES

Amir, A.D., K.L. Davis, M.D. Tadmor, E.F. Simonds, J.H. Levine, S.C. Bendall, D.K. Shenfeld, S. Krishnaswamy, G.P. Nolan, and D. Pe'er. 2013. viSNE enables visualization of high dimensional single-cell data and reveals phenotypic heterogeneity of leukemia. *Nat. Biotechnol.* 31:545–552.

Anderson, K.G., K. Mayer-Barber, H. Sung, L. Beura, B.R. James, J.J. Taylor, L. Qunaj, T.S. Griffith, V. Vezys, D.L. Barber, and D. Masopust. 2014.

Intravascular staining for discrimination of vascular and tissue leukocytes. *Nat. Protoc.* 9:209–222. http://dx.doi.org/10.1038/nprot.2014.005

Auffray, C., D. Fogg, M. Garfa, G. Elain, O. Join-Lambert, S. Kayal, S. Sarnacki, A. Cumano, G. Lauvau, and F. Geissmann. 2007. Monitoring of blood vessels and tissues by a population of monocytes with patrolling behavior. *Science.* 317:666–670. http://dx.doi.org/10.1126/science.1142883

Balabanian, K., E. Brotin, V. Biajoux, L. Bouchet-Delbos, E. Lainey, O. Fenneteau, D. Bonnet, L. Fiette, D. Emilie, and F. Bachelerie. 2012. Proper desensitization of CXCR4 is required for lymphocyte development and peripheral compartmentalization in mice. *Blood.* 119:5722–5730. http://dx.doi.org/10.1182/blood-2012-01-403378

Bar-Joseph, Z., D.K. Gifford, and T.S. Jaakkola. 2001. Fast optimal leaf ordering for hierarchical clustering. *Bioinformatics.* 17:S22–S29. http://dx.doi.org/10.1093/bioinformatics/17.suppl_1.S22

Beaussant Cohen, S., O. Fenneteau, E. Plouvier, P.S. Rohrlich, G. Daltroff, I. Plantier, A. Dupuy, D. Kerob, B. Beaupain, P. Bordigoni, et al. 2012. Description and outcome of a cohort of 8 patients with WHIM syndrome from the French Severe Chronic Neutropenia Registry. *Orphanet J. Rare Dis.* 7:71. http://dx.doi.org/10.1186/1750-1172-7-71

Becher, B., A. Schlitzer, J. Chen, F. Mair, H.R. Sumatoh, K.W. Teng, D. Low, C. Ruedl, P. Riccardi-Castagnoli, M. Poidinger, et al. 2014. High-dimensional analysis of the murine myeloid cell system. *Nat. Immunol.* 15:1181–1189. http://dx.doi.org/10.1038/ni.3006

Bendall, S.C., K.L. Davis, A.D. Amir, M.D. Tadmor, E.F. Simonds, T.J. Chen, D.K. Shenfeld, G.P. Nolan, and D. Pe'er. 2014. Single-cell trajectory detection uncovers progression and regulatory coordination in human B cell development. *Cell.* 157:714–725. http://dx.doi.org/10.1016/j.cell.2014.04.005

Bierman, H.R., K.H. Kelly, F.L. Cordes, R.L. Byron Jr., J.A. Polhemus, and S. Rappoport. 1952. The release of leukocytes and platelets from the pulmonary circulation by epinephrine. *Blood.* 7:683–692.

Carlin, L.M., E.G. Stamatiades, C. Auffray, R.N. Hanna, L. Glover, G. Vizcay-Barrena, C.C. Hedrick, H.T. Cook, S. Diebold, and F. Geissmann. 2013. Nr4a1-dependent Ly6C(low) monocytes monitor endothelial cells and orchestrate their disposal. *Cell.* 153:362–375. http://dx.doi.org/10.1016/j.cell.2013.03.010

Chen, Q., M. Khoury, G. Limmon, M. Choolani, J.K. Chan, and J. Chen. 2013. Human fetal hepatic progenitor cells are distinct from, but closely related to, hematopoietic stem/progenitor cells. *Stem Cells.* 31:1160–1169. http://dx.doi.org/10.1002/stem.1359

Clausen, B.E., C. Burkhardt, W. Reith, R. Renkawitz, and I. Förster. 1999. Conditional gene targeting in macrophages and granulocytes using LysMcre mice. *Transgenic Res.* 8:265–277. http://dx.doi.org/10.1023/A:1008942828960

Cros, J., N. Cagnard, K. Woollard, N. Patey, S.Y. Zhang, B. Senechal, A. Puel, S.K. Biswas, D. Moshous, C. Picard, et al. 2010. Human CD14dim monocytes patrol and sense nucleic acids and viruses via TLR7 and TLR8 receptors. *Immunity.* 33:375–386. http://dx.doi.org/10.1016/j.immuni.2010.08.012

Devi, S., Y. Wang, W.K. Chew, R. Lima, N. A-González, C.N. Mattar, S.Z. Chong, A. Schlitzer, N. Bakocevic, S. Chew, et al. 2013. Neutrophil mobilization via plerixafor-mediated CXCR4 inhibition arises from lung demargination and blockade of neutrophil homing to the bone marrow. *J. Exp. Med.* 210:2321–2336. http://dx.doi.org/10.1084/jem.20130056

Dhaliwal, K., E. Scholefield, D. Ferenbach, M. Gibbons, R. Duffin, D.A. Dorward, A.C. Morris, D. Humphries, A. MacKinnon, T.S. Wilkinson, et al. 2012. Monocytes control second-phase neutrophil emigration in established lipopolysaccharide-induced murine lung injury. *Am. J. Respir. Crit. Care Med.* 186:514–524. http://dx.doi.org/10.1164/rccm.201112-2132OC

Doerschuk, C.M., N. Beyers, H.O. Coxson, B. Wiggs, and J.C. Hogg. 1993. Comparison of neutrophil and capillary diameters and their relation to neutrophil sequestration in the lung. *J. Appl. Physiol.* 74:3040–3045.

Drummond, S., S. Ramachandran, E. Torres, J. Huang, D. Hehre, C. Suguihara, and K.C. Young. 2015. CXCR4 blockade attenuates hyperoxia-induced lung injury in neonatal rats. *Neonatology.* 107:304–311. http://dx.doi.org/10.1159/000371835

Eash, K.J., J.M. Means, D.W. White, and D.C. Link. 2009. CXCR4 is a key regulator of neutrophil release from the bone marrow under basal and stress granulopoiesis conditions. *Blood.* 113:4711–4719. http://dx.doi.org/10.1182/blood-2008-09-177287

Evrard, M., S.Z. Chong, S. Devi, W.K. Chew, B. Lee, M. Poidinger, F. Ginhoux, S.M. Tan, and L.G. Ng. 2015. Visualization of bone marrow monocyte mobilization using Cx3cr1gfp/+Flt3L-/- reporter mouse by multiphoton intravital microscopy. *J. Leukoc. Biol.* 97:611–619. http://dx.doi.org/10.1189/jlb.1TA0514-274R

Ginhoux, F., and S. Jung. 2014. Monocytes and macrophages: developmental pathways and tissue homeostasis. *Nat. Rev. Immunol.* 14:392–404. http://dx.doi.org/10.1038/nri3671

Goto, Y., J.C. Hogg, T. Suwa, K.B. Quinlan, and S.F. van Eeden. 2003. A novel method to quantify the turnover and release of monocytes from the bone marrow using the thymidine analog 5′-bromo-2′-deoxyuridine. *Am. J. Physiol. Cell Physiol.* 285:C253–C259. http://dx.doi.org/10.1152/ajpcell.00035.2003

Gulino, A.V., D. Moratto, S. Sozzani, P. Cavadini, K. Otero, L. Tassone, L. Imberti, S. Pirovano, L.D. Notarangelo, R. Soresina, et al. 2004. Altered leukocyte response to CXCL12 in patients with warts hypogammaglobulinemia, infections, myelokathexis (WHIM) syndrome. *Blood.* 104:444–452. http://dx.doi.org/10.1182/blood-2003-10-3532

Hahsler, M., K. Hornik, and C. Buchta. 2008. Getting things in order: an introduction to the R package seriation. *J. Stat. Softw.* 25:1–34. http://dx.doi.org/10.18637/jss.v025.i03

Hanna, R.N., L.M. Carlin, H.G. Hubbeling, D. Nackiewicz, A.M. Green, J.A. Punt, F. Geissmann, and C.C. Hedrick. 2011. The transcription factor NR4A1 (Nur77) controls bone marrow differentiation and the survival of Ly6C$^-$ monocytes. *Nat. Immunol.* 12:778–785. http://dx.doi.org/10.1038/ni.2063

Hanna, R.N., C. Cekic, D. Sag, R. Tacke, G.D. Thomas, H. Nowyhed, E. Herrley, N. Rasquinha, S. McArdle, R. Wu, et al. 2015. Patrolling monocytes control tumor metastasis to the lung. *Science.* 350:985–990. http://dx.doi.org/10.1126/science.aac9407

Hashimoto, D., A. Chow, C. Noizat, P. Teo, M.B. Beasley, M. Leboeuf, C.D. Becker, P. See, J. Price, D. Lucas, et al. 2013. Tissue-resident macrophages self-maintain locally throughout adult life with minimal contribution from circulating monocytes. *Immunity.* 38:792–804. http://dx.doi.org/10.1016/j.immuni.2013.04.004

Hernandez, P.A., R.J. Gorlin, J.N. Lukens, S. Taniuchi, J. Bohinjec, F. Francois, M.E. Klotman, and G.A. Diaz. 2003. Mutations in the chemokine receptor gene CXCR4 are associated with WHIM syndrome, a combined immunodeficiency disease. *Nat. Genet.* 34:70–74. http://dx.doi.org/10.1038/ng1149

Hettinger, J., D.M. Richards, J. Hansson, M.M. Barra, A.C. Joschko, J. Krijgsveld, and M. Feuerer. 2013. Origin of monocytes and macrophages in a committed progenitor. *Nat. Immunol.* 14:821–830. http://dx.doi.org/10.1038/ni.2638

Hogg, J.C. 1987. Neutrophil kinetics and lung injury. *Physiol. Rev.* 67:1249–1295.

Ingersoll, M.A., R. Spanbroek, C. Lottaz, E.L. Gautier, M. Frankenberger, R. Hoffmann, R. Lang, M. Haniffa, M. Collin, F. Tacke, et al. 2010. Comparison of gene expression profiles between human and mouse monocyte subsets. *Blood.* 115:e10–e19. http://dx.doi.org/10.1182/blood-2009-07-235028

Inra, C.N., B.O. Zhou, M. Acar, M.M. Murphy, J. Richardson, Z. Zhao, and S.J. Morrison. 2015. A perisinusoidal niche for extramedullary haematopoiesis in the spleen. *Nature.* 527:466–471. http://dx.doi.org/10.1038/nature15530

Jacquelin, S., F. Licata, K. Dorgham, P. Hermand, L. Poupel, E. Guyon, P. Deterre, D.A. Hume, C. Combadière, and A. Boissonnas. 2013. CX3CR1 reduces Ly6Chigh-monocyte motility within and release from the bone marrow after chemotherapy in mice. *Blood*. 122:674–683. http://dx.doi.org/10.1182/blood-2013-01-480749

Jung, H., D.S. Mithal, J.E. Park, and R.J. Miller. 2015. Localized CCR2 Activation in the Bone Marrow Niche Mobilizes Monocytes by Desensitizing CXCR4. *PLoS One.* 10:e0128387. http://dx.doi.org/10.1371/journal.pone.0128387

Kreisel, D., R.G. Nava, W. Li, B.H. Zinselmeyer, B. Wang, J. Lai, R. Pless, A.E. Gelman, A.S. Krupnick, and M.J. Miller. 2010. In vivo two-photon imaging reveals monocyte-dependent neutrophil extravasation during pulmonary inflammation. *Proc. Natl. Acad. Sci. USA*. 107:18073–18078. http://dx.doi.org/10.1073/pnas.1008737107

Kuebler, W.M., and A.E. Goetz. 2002. The marginated pool. *Eur. Surg. Res.* 34:92–100. http://dx.doi.org/10.1159/000048894

Lamb, J., E.D. Crawford, D. Peck, J.W. Modell, I.C. Blat, M.J. Wrobel, J. Lerner, J.P. Brunet, A. Subramanian, K.N. Ross, et al. 2006. The Connectivity Map: using gene-expression signatures to connect small molecules, genes, and disease. *Science.* 313:1929–1935. http://dx.doi.org/10.1126/science.1132939

Landsman, L., L. Bar-On, A. Zernecke, K.W. Kim, R. Krauthgamer, E. Shagdarsuren, S.A. Lira, I.L. Weissman, C. Weber, and S. Jung. 2009. CX3CR1 is required for monocyte homeostasis and atherogenesis by promoting cell survival. *Blood*. 113:963–972. http://dx.doi.org/10.1182/blood-2008-07-170787

Leuschner, F., P. Dutta, R. Gorbatov, T.I. Novobrantseva, J.S. Donahoe, G. Courties, K.M. Lee, J.I. Kim, J.F. Markmann, B. Marinelli, et al. 2011. Therapeutic siRNA silencing in inflammatory monocytes in mice. *Nat. Biotechnol.* 29:1005–1010. http://dx.doi.org/10.1038/nbt.1989

Leuschner, F., P.J. Rauch, T. Ueno, R. Gorbatov, B. Marinelli, W.W. Lee, P. Dutta, Y. Wei, C. Robbins, Y. Iwamoto, et al. 2012. Rapid monocyte kinetics in acute myocardial infarction are sustained by extramedullary monocytopoiesis. *J. Exp. Med.* 209:123–137. http://dx.doi.org/10.1084/jem.20111009

Liu, Q., Z. Li, J.L. Gao, W. Wan, S. Ganesan, D.H. McDermott, and P.M. Murphy. 2015. CXCR4 antagonist AMD3100 redistributes leukocytes from primary immune organs to secondary immune organs, lung, and blood in mice. *Eur. J. Immunol.* 45:1855–1867. http://dx.doi.org/10.1002/eji.201445245

Looney, M.R., and J. Bhattacharya. 2014. Live imaging of the lung. *Annu. Rev. Physiol.* 76:431–445. http://dx.doi.org/10.1146/annurev-physiol-021113-170331

Looney, M.R., E.E. Thornton, D. Sen, W.J. Lamm, R.W. Glenny, and M.F. Krummel. 2011. Stabilized imaging of immune surveillance in the mouse lung. *Nat. Methods.* 8:91–96. http://dx.doi.org/10.1038/nmeth.1543

Lukacs, N.W., A. Berlin, D. Schols, R.T. Skerlj, and G.J. Bridger. 2002. AMD3100, a CxCR4 antagonist, attenuates allergic lung inflammation and airway hyperreactivity. *Am. J. Pathol.* 160:1353–1360. http://dx.doi.org/10.1016/S0002-9440(10)62562-X

MacNee, W., and C. Selby. 1993. New perspectives on basic mechanisms in lung disease. 2. Neutrophil traffic in the lungs: role of haemodynamics, cell adhesion, and deformability. *Thorax*. 48:79–88. http://dx.doi.org/10.1136/thx.48.1.79

Majmudar, M.D., E.J. Keliher, T. Heidt, F. Leuschner, J. Truelove, B.F. Sena, R. Gorbatov, Y. Iwamoto, P. Dutta, G. Wojtkiewicz, et al. 2013. Monocyte-directed RNAi targeting CCR2 improves infarct healing in atherosclerosis-prone mice. *Circulation*. 127:2038–2046. http://dx.doi.org/10.1161/CIRCULATIONAHA.112.000116

Martin, B.A., J.L. Wright, H. Thommasen, and J.C. Hogg. 1982. Effect of pulmonary blood flow on the exchange between the circulating and marginating pool of polymorphonuclear leukocytes in dog lungs. *J. Clin. Invest.* 69:1277–1285. http://dx.doi.org/10.1172/JCI110567

Martin, C., P.C. Burdon, G. Bridger, J.C. Gutierrez-Ramos, T.J. Williams, and S.M. Rankin. 2003. Chemokines acting via CXCR2 and CXCR4 control the release of neutrophils from the bone marrow and their return following senescence. *Immunity.* 19:583–593. http://dx.doi.org/10.1016/S1074-7613(03)00263-2

McDermott, D.H., Q. Liu, D. Velez, L. Lopez, S. Anaya-O'Brien, J. Ulrick, N. Kwatemaa, J. Starling, T.A. Fleisher, D.A. Priel, et al. 2014. A phase 1 clinical trial of long-term, low-dose treatment of WHIM syndrome with the CXCR4 antagonist plerixafor. *Blood*. 123:2308–2316. http://dx.doi.org/10.1182/blood-2013-09-527226

Mildner, A., S. Yona, and S. Jung. 2013. A close encounter of the third kind: monocyte-derived cells. *Adv. Immunol.* 120:69–103. http://dx.doi.org/10.1016/B978-0-12-417028-5.00003-X

Nagasawa, T. 2014. CXC chemokine ligand 12 (CXCL12) and its receptor CXCR4. *J. Mol. Med.* 92:433–439. http://dx.doi.org/10.1007/s00109-014-1123-8

Nahrendorf, M., M.J. Pittet, and F.K. Swirski. 2010. Monocytes: protagonists of infarct inflammation and repair after myocardial infarction. *Circulation*. 121:2437–2445. http://dx.doi.org/10.1161/CIRCULATIONAHA.109.916346

Ng, L.G., J.S. Qin, B. Roediger, Y. Wang, R. Jain, L.L. Cavanagh, A.L. Smith, C.A. Jones, M. de Veer, M.A. Grimbaldeston, et al. 2011. Visualizing the neutrophil response to sterile tissue injury in mouse dermis reveals a three-phase cascade of events. *J. Invest. Dermatol.* 131:2058–2068. http://dx.doi.org/10.1038/jid.2011.179

Nguyen, K.D., S.J. Fentress, Y. Qiu, K. Yun, J.S. Cox, and A. Chawla. 2013. Circadian gene Bmal1 regulates diurnal oscillations of Ly6C(hi) inflammatory monocytes. *Science.* 341:1483–1488. http://dx.doi.org/10.1126/science.1240636

O'Dea, K.P., M.R. Wilson, J.O. Dokpesi, K. Wakabayashi, L. Tatton, N. van Rooijen, and M. Takata. 2009. Mobilization and margination of bone marrow Gr-1high monocytes during subclinical endotoxemia predisposes the lungs toward acute injury. *J. Immunol.* 182:1155–1166. http://dx.doi.org/10.4049/jimmunol.182.2.1155

Ogawa, M., Y. Matsuzaki, S. Nishikawa, S. Hayashi, T. Kunisada, T. Sudo, T. Kina, H. Nakauchi, and S. Nishikawa. 1991. Expression and function of c-kit in hemopoietic progenitor cells. *J. Exp. Med.* 174:63–71. http://dx.doi.org/10.1084/jem.174.1.63

Picelli, S., O.R. Faridani, A.K. Björklund, G. Winberg, S. Sagasser, and R. Sandberg. 2014. Full-length RNA-seq from single cells using Smart-seq2. *Nat. Protoc.* 9:171–181. http://dx.doi.org/10.1038/nprot.2014.006

Poupel, L., A. Boissonnas, P. Hermand, K. Dorgham, E. Guyon, C. Auvynet, F.S. Charles, P. Lesnik, P. Deterre, and C. Combadiere. 2013. Pharmacological inhibition of the chemokine receptor, CX3CR1, reduces atherosclerosis in mice. *Arterioscler. Thromb. Vasc. Biol.* 33:2297–2305. http://dx.doi.org/10.1161/ATVBAHA.112.300930

Reutershan, J., A. Basit, E.V. Galkina, and K. Ley. 2005. Sequential recruitment of neutrophils into lung and bronchoalveolar lavage fluid in LPS-induced acute lung injury. *Am. J. Physiol. Lung Cell. Mol. Physiol.* 289:L807–L815. http://dx.doi.org/10.1152/ajplung.00477.2004

Rittirsch, D., M.S. Huber-Lang, M.A. Flierl, and P.A. Ward. 2009. Immunodesign of experimental sepsis by cecal ligation and puncture. *Nat. Protoc.* 4:31–36. http://dx.doi.org/10.1038/nprot.2008.214

Robbins, C.S., A. Chudnovskiy, P.J. Rauch, J.L. Figueiredo, Y. Iwamoto, R. Gorbatov, M. Etzrodt, G.F. Weber, T. Ueno, N. van Rooijen, et al. 2012. Extramedullary hematopoiesis generates Ly-6C(high) monocytes that infiltrate atherosclerotic lesions. *Circulation*. 125:364–374. http://dx.doi.org/10.1161/CIRCULATIONAHA.111.061986

Sakaue-Sawano, A., T. Hoshida, M. Yo, R. Takahashi, K. Ohtawa, T. Arai, E. Takahashi, S. Noda, H. Miyoshi, and A. Miyawaki. 2013. Visualizing

developmentally programmed endoreplication in mammals using ubiquitin oscillators. *Development*. 140:4624–4632. http://dx.doi.org/10.1242/dev.099226

Scheiermann, C., Y. Kunisaki, and P.S. Frenette. 2013. Circadian control of the immune system. *Nat. Rev. Immunol*. 13:190–198. http://dx.doi.org/10.1038/nri3386

Segura, E., and S. Amigorena. 2013. Inflammatory dendritic cells in mice and humans. *Trends Immunol*. 34:440–445. http://dx.doi.org/10.1016/j.it.2013.06.001

Serbina, N.V., and E.G. Pamer. 2006. Monocyte emigration from bone marrow during bacterial infection requires signals mediated by chemokine receptor CCR2. *Nat. Immunol*. 7:311–317. http://dx.doi.org/10.1038/ni1309

Serbina, N.V., T. Jia, T.M. Hohl, and E.G. Pamer. 2008. Monocyte-mediated defense against microbial pathogens. *Annu. Rev. Immunol*. 26:421–452. http://dx.doi.org/10.1146/annurev.immunol.26.021607.090326

Shi, C., and E.G. Pamer. 2011. Monocyte recruitment during infection and inflammation. *Nat. Rev. Immunol*. 11:762–774. http://dx.doi.org/10.1038/nri3070

Shi, C., T. Jia, S. Mendez-Ferrer, T.M. Hohl, N.V. Serbina, L. Lipuma, I. Leiner, M.O. Li, P.S. Frenette, and E.G. Pamer. 2011. Bone marrow mesenchymal stem and progenitor cells induce monocyte emigration in response to circulating toll-like receptor ligands. *Immunity*. 34:590–601. http://dx.doi.org/10.1016/j.immuni.2011.02.016

Staub, N.C., and E.L. Schultz. 1968. Pulmonary capillary length in dogs, cat and rabbit. *Respir. Physiol*. 5:371–378. http://dx.doi.org/10.1016/0034-5687(68)90028-5

Suratt, B.T., J.M. Petty, S.K. Young, K.C. Malcolm, J.G. Lieber, J.A. Nick, J.A. Gonzalo, P.M. Henson, and G.S. Worthen. 2004. Role of the CXCR4/SDF-1 chemokine axis in circulating neutrophil homeostasis. *Blood*. 104:565–571. http://dx.doi.org/10.1182/blood-2003-10-3638

Swirski, F.K., M. Nahrendorf, M. Etzrodt, M. Wildgruber, V. Cortez-Retamozo, P. Panizzi, J.L. Figueiredo, R.H. Kohler, A. Chudnovskiy, P. Waterman, et al. 2009. Identification of splenic reservoir monocytes and their deployment to inflammatory sites. *Science*. 325:612–616. http://dx.doi.org/10.1126/science.1175202

Tacke, F., D. Alvarez, T.J. Kaplan, C. Jakubzick, R. Spanbroek, J. Llodra, A. Garin, J. Liu, M. Mack, N. van Rooijen, et al. 2007. Monocyte subsets differentially employ CCR2, CCR5, and CX3CR1 to accumulate within atherosclerotic plaques. *J. Clin. Invest*. 117:185–194. http://dx.doi.org/10.1172/JCI28549

Terashima, T., B. Wiggs, D. English, J.C. Hogg, and S.F. van Eeden. 1996. Polymorphonuclear leukocyte transit times in bone marrow during streptococcal pneumonia. *Am. J. Physiol*. 271:L587–L592.

Thomas, G., R. Tacke, C.C. Hedrick, and R.N. Hanna. 2015. Nonclassical patrolling monocyte function in the vasculature. *Arterioscler. Thromb. Vasc. Biol*. 35:1306–1316. http://dx.doi.org/10.1161/ATVBAHA.114.304650

van Furth, R., and W. Sluiter. 1986. Distribution of blood monocytes between a marginating and a circulating pool. *J. Exp. Med*. 163:474–479. http://dx.doi.org/10.1084/jem.163.2.474

van Furth, R., J.A. Raeburn, and T.L. van Zwet. 1979. Characteristics of human mononuclear phagocytes. *Blood*. 54:485–500.

Varol, C., L. Landsman, D.K. Fogg, L. Greenshtein, B. Gildor, R. Margalit, V. Kalchenko, F. Geissmann, and S. Jung. 2007. Monocytes give rise to mucosal, but not splenic, conventional dendritic cells. *J. Exp. Med*. 204:171–180. http://dx.doi.org/10.1084/jem.20061011

Varol, C., A. Mildner, and S. Jung. 2015. Macrophages: development and tissue specialization. *Annu. Rev. Immunol*. 33:643–675. http://dx.doi.org/10.1146/annurev-immunol-032414-112220

Wang, Y., L. Cui, W. Gonsiorek, S.H. Min, G. Anilkumar, S. Rosenblum, J. Kozlowski, D. Lundell, J.S. Fine, and E.P. Grant. 2009. CCR2 and CXCR4 regulate peripheral blood monocyte pharmacodynamics and link to efficacy in experimental autoimmune encephalomyelitis. *J. Inflamm. (Lond.)*. 6:32. http://dx.doi.org/10.1186/1476-9255-6-32

Weber, G.F., B.G. Chousterman, S. He, A.M. Fenn, M. Nairz, A. Anzai, T. Brenner, F. Uhle, Y. Iwamoto, C.S. Robbins, et al. 2015. Interleukin-3 amplifies acute inflammation and is a potential therapeutic target in sepsis. *Science*. 347:1260–1265. http://dx.doi.org/10.1126/science.aaa4268

Wong, K.L., J.J. Tai, W.C. Wong, H. Han, X. Sem, W.H. Yeap, P. Kourilsky, and S.C. Wong. 2011. Gene expression profiling reveals the defining features of the classical, intermediate, and nonclassical human monocyte subsets. *Blood*. 118:e16–e31. http://dx.doi.org/10.1182/blood-2010-12-326355

Yona, S., K.W. Kim, Y. Wolf, A. Mildner, D. Varol, M. Breker, D. Strauss-Ayali, S. Viukov, M. Guilliams, A. Misharin, et al. 2013. Fate mapping reveals origins and dynamics of monocytes and tissue macrophages under homeostasis. *Immunity*. 38:79–91. http://dx.doi.org/10.1016/j.immuni.2012.12.001

SUPPLEMENTAL MATERIAL

Chong et al., http://dx.doi.org/10.1084/jem.20160800

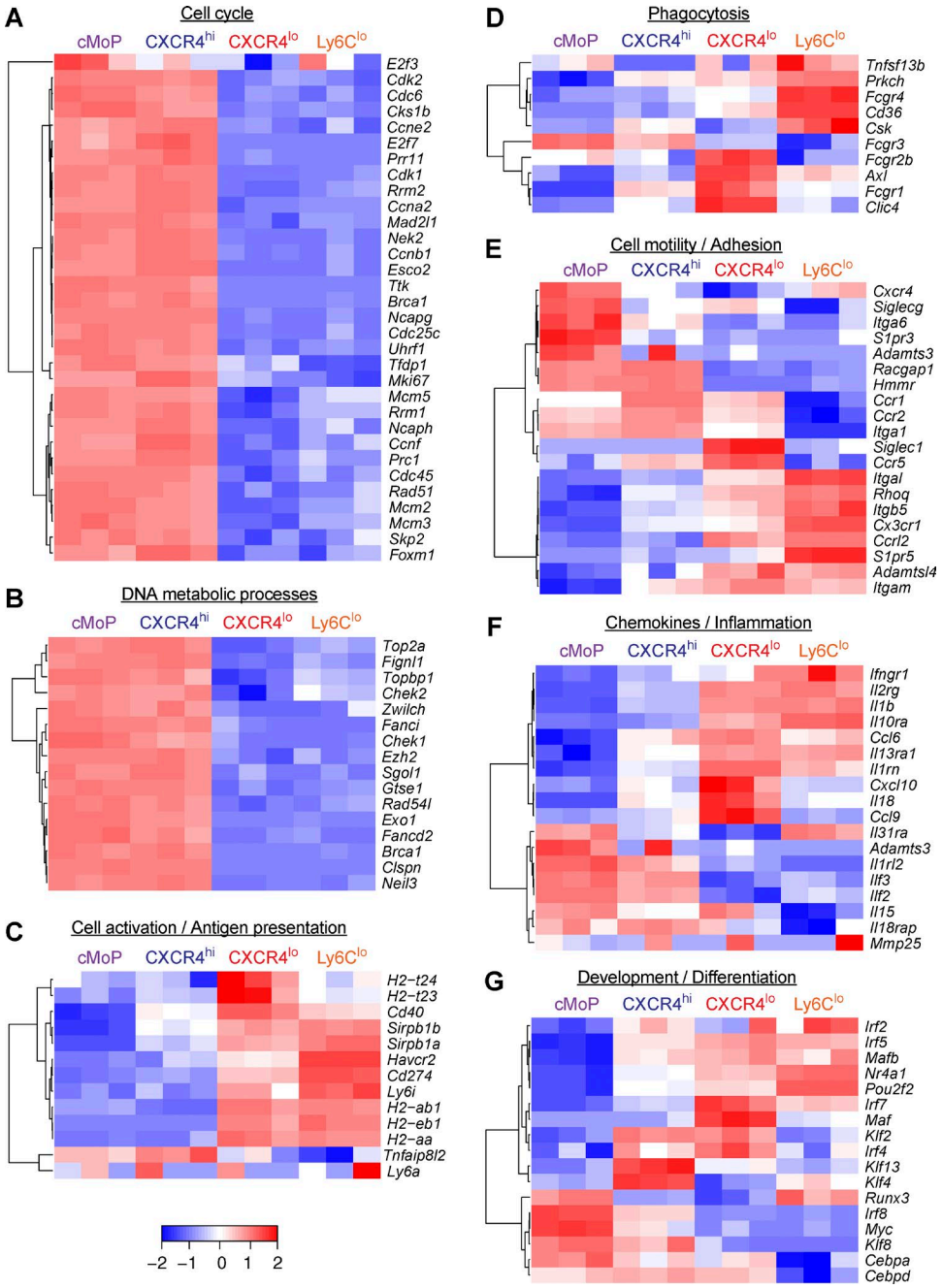

Figure S1. **Heatmaps of genes between cell subsets of the monocyte developmental pathway.** (A–G) NGS was performed on RNA extracted from sorted BM cMoPs, CXCR4^{hi} and CXCR4^{lo} Ly6C^{hi} monocytes and Ly6C^{lo} monocytes from three individual mice. Heat maps showing genes that are involved in cell cycle (A), DNA metabolic processes (B), cell activation and antigen presentation (C), phagocytosis (D), cell motility and adhesion (E), chemokines and inflammation (F) and development and differentiation (G).

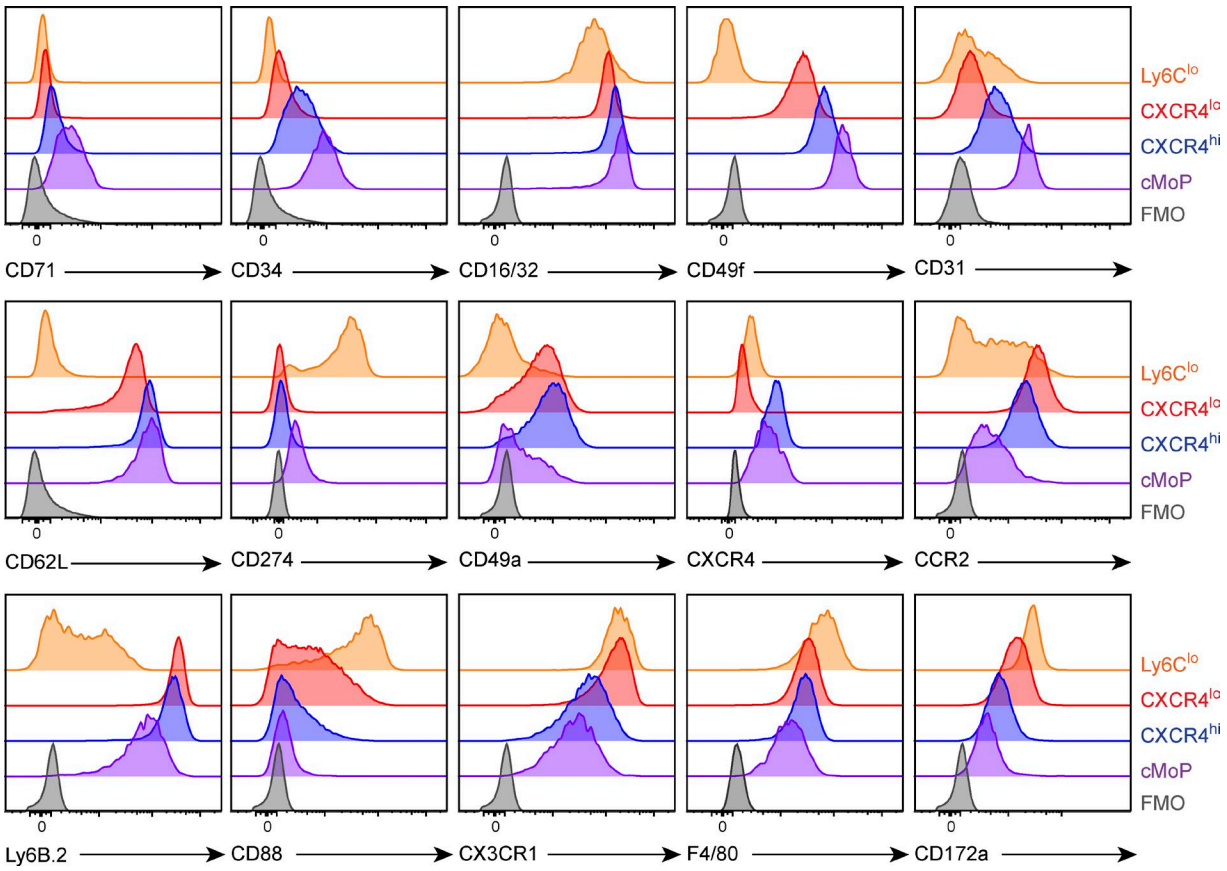

Figure S2. **Cell surface marker expression for distinguishing monocyte subsets.** Flow cytometry was performed on BM cMoPs, CXCR4^{hi} and CXCR4^{lo} Ly6C^{hi} monocytes and Ly6C^{lo} monocytes for the analysis of indicated surface markers. Results are representative of one out of two independent experiments.

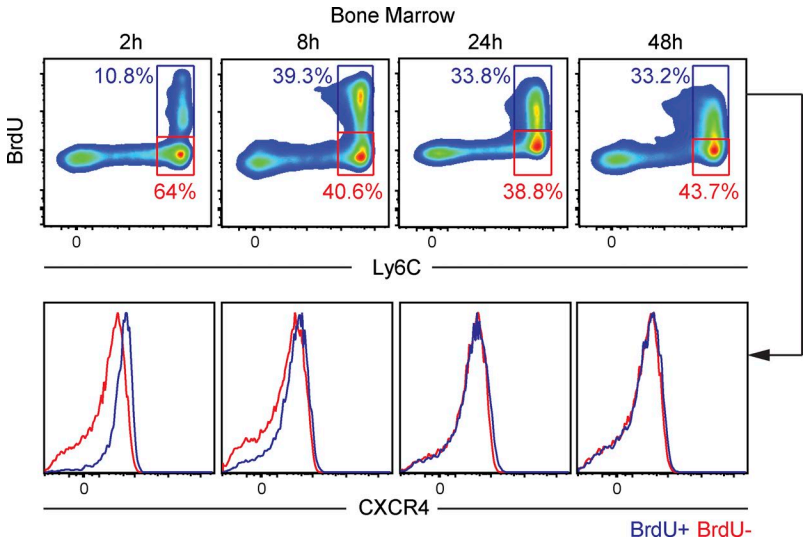

Figure S3. **Gating strategy for the analysis of CXCR4 expression on BM Ly6C^{hi} monocytes.** Representative flow cytometry plots showing progressive BrdU incorporation into BM Ly6C^{hi} monocytes (*top panels*) and subsequent gating for CXCR4 expression (*bottom panels*) of BrdU^{+} cells (*red box*), BrdU^{-} cells (*blue box*; n = 4–5 mice per group). Results representative of one out of two independent experiments.

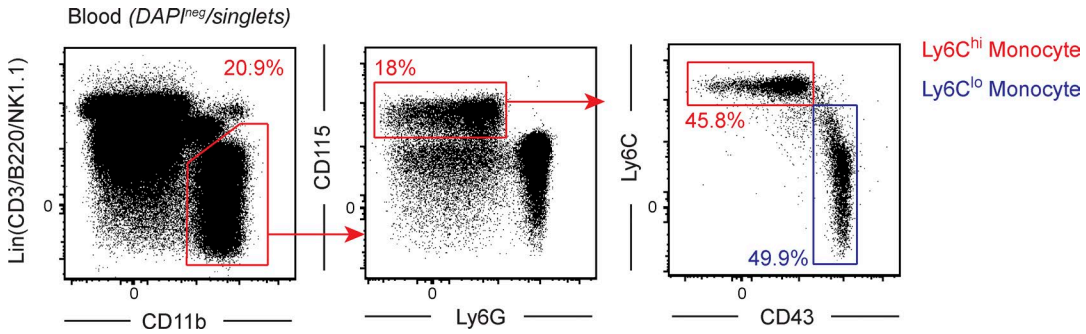

Figure S4. **Gating strategy of blood monocytes in mice.** Gating strategy for blood monocytes (pregated on DAPI^{neg}/singlets). Monocytes are defined as Lin(CD3/B220/NK1.1)$^{-}$CD115^{+}Ly6G^{-}CD11b^{+} and Ly6C^{hi}CD43^{-} or Ly6C^{lo}CD43^{+} according to the subset. Flow cytometry plots are representative of one out of at least three independent experiments.

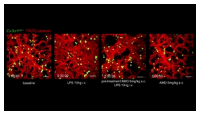

Video 1. **Monocyte margination in the pulmonary vasculature.** Time-lapse image sequence of maximum intensity projection displaying the behavior of GFP^{+} cells in the lungs (alveolar space) of *Cx3cr1*$^{gfp/+}$ mice. TRITC-dextran (250 µg) was administered i.v. to delineate the lung vasculature. Shown are the motility patterns of GFP^{+} monocytes at baseline and after treatment with LPS (10 ng), AMD3100 (5 mg/kg), or LPS and AMD3100 together. For mice treated with LPS, monocytes are observed to reduce their speed and increase duration of adherence in the lung endothelium. This phenomenon was abolished when mice were pretreated with AMD3100. Videos are representative of 3 mice per treatment. Elapsed time is shown as hours:minutes:seconds. Scale bar: 50 µm.

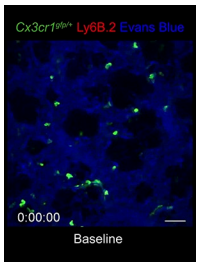

Video 2. **Visualization of Ly6C^{hi} monocytes in *Cx3cr1*$^{gfp/+}$ mice with an anti–Ly6B.2 antibody.** Time-lapse image sequence of maximum intensity projection displaying the behavior of GFP^{+} cells in the lungs (alveolar space) of *Cx3cr1*$^{gfp/+}$ mice. Evans blue (50 µg) was administered i.v. to delineate the lung vasculature. 5 min after the beginning of imaging, Ly6B.2-PE (4 µg) was injected i.v., and allowed the visualization of Ly6C^{hi} monocytes (Ly6B.2^{+}CX$_3$CR1^{+}), Ly6C^{lo} monocytes (Ly6B.2^{-}CX$_3$CR1^{+}) and neutrophils (Ly6B.2^{+}CX$_3$CR1^{-}). Video is representative of 3 mice. Elapsed time is shown as hours:minutes:seconds. Scale bar: 40 µm.